LITHOS 424-425 (2022) 106775

Contents lists available at ScienceDirect

LITHOS

journal homepage: www.elsevier.com/locate/lithos

Porphyry Cu fertility of eastern Paleo-Tethyan arc magmas: Evidence from zircon and apatite compositions

Jing-Jing Zhu [a,*], Ruizhong Hu [a,b], Xian-Wu Bi [a,b], Pete Hollings [c], Hong Zhong [a,b], Jian-Feng Gao [a], Li-Chuan Pan [a], Ming-Liang Huang [a], Dian-Zhong Wang [a]

[a] State Key Laboratory of Ore Deposit Geochemistry, Institute of Geochemistry, Chinese Academy of Sciences, Guiyang 550081, China
[b] College of Earth and Planetary Sciences, University of Chinese Academy of Sciences, Beijing 100049, China
[c] Department of Geology, Lakehead University, 955 Oliver Road, Thunder Bay P7B 5E1, Canada

ARTICLE INFO

Keywords:
Paleo-Tethyan arc magmas
Porphyry Cu fertility
Magmatic oxygen fugacity
Zircon and apatite

ABSTRACT

The Paleo-Tethyan arc belt is host to a small number of porphyry Cu deposits the key controls on which remains poorly understood. It has been hypothesized that the Paleo-Tethyan arc magmas were reduced and therefore less fertile for porphyry Cu formation but few studies have been conducted to directly assess the magmatic oxygen fugacity. We investigate the magma fertility of eastern Paleo-Tethyan arc igneous rocks in the Sanjiang region, SW China, represented by the Maoding (268.3 ± 2.3 Ma), Suwalong (275.6 ± 1.4 Ma to 264.7 ± 1.4 Ma) and Baimaxueshan (255.7 ± 1.5 Ma to 249.3 ± 1.1 Ma) granitoids. They have geochemical features consistent with typical continental arc rocks, formed from partial melting of the mantle wedge, with increasing contamination of crust-derived melts over time. The presence of amphibole, high Sr/Y ratios (35 ± 20, n = 17), and lack of negative Eu anomalies (Eu_N/Eu_N^* = 1.04 ± 0.3, n = 17) are consistent with derivation from hydrous magmas. Zircons from the intrusive rocks have relatively low Eu_N/Eu_N^* (mostly <0.4) ratios and calculated ΔFMQ values (−2.1 ± 1.2, n = 86). Combined with apatite microphenocrysts with extremely low sulfur contents (< 0.12 wt% SO_3), it suggests that the intrusions originated from water-rich but reduced arc magmas, that were less fertile for porphyry Cu formation. Our study highlights that magmatic fO_2 is probably a critical control on the prospectivity of arc systems and confirms that zircon and apatite compositions can be used to evaluate porphyry Cu fertility.

1. Introduction

The genetic link between subduction, arc magma fertility, and the formation of porphyry Cu ± Au ± Mo deposits has been widely discussed in recent decades (Cooke et al., 2005; Richards, 2003; Sillitoe, 2010; Sun et al., 2015). In general, arc magmas are moderately oxidized (ΔFMQ +1 to +2, where ΔFMQ is the value relative to fayalite-magnetite-quartz buffer in log fO_2 units), are enriched in water (> 4 wt%), sulfur (>1000 ppm), and chlorine (>3000 ppm), and are derived from the continuous dehydration of subducted oceanic slabs (Evans and Tomkins, 2011; Kelley and Cottrell, 2009; Richards, 2015a). These magmas allow the transport of economically important metals (Cu and Au) in the melts and the subsequently exsolved hydrothermal fluids, potentially leading to the formation of sulfide-rich ores (Audétát and Simon, 2012; Hou et al., 2015; Zhu et al., 2018).

Arc magmas generally have the potential to form porphyry deposits, but not all magmatic arcs host economic porphyry Cu deposits (Richards, 2003). Possible reasons for this include poor preservation, reduced magmas that result in early sulfide saturation and chalcophile metal loss, and lack of a focus for hydrothermal fluids (Richards, 2013; Sillitoe, 2018). The Paleo-Tethyan arc which stretches for over 10,000 km from the Carpathians–Balkans, through Turkey, Iran, Pakistan, Tibet–Sanjiang Region of southwest China, and IndoChina is host to only a small number of porphyry Cu deposits (Richards, 2015b; Richards and Şengör, 2017). Richards and Şengör (2017) suggested that the lack of porphyry Cu deposits may be attributed to the presence of reduced arc magmas, as the Paleo-Tethyan Ocean was closed during the Permian and thus isolated from global oceanic circulation. However, others have argued that the Paleotethys was an open ocean and not anoxic, which would lead to a higher potential for porphyry Cu deposits in the Paleo-Tethyan arc belt (Wang et al., 2020; Yang et al., 2011). The competing views are possible because of the limited number of studies that directly constrain the magma fertility, particularly the oxidation state (fO_2) of the Paleo-Tethyan arc magmas. It is difficult to evaluate magmatic fO_2

* Corresponding author.
E-mail address: zhujingjing@vip.gyig.ac.cn (J.-J. Zhu).

https://doi.org/10.1016/j.lithos.2022.106775
Received 11 April 2022; Received in revised form 14 June 2022; Accepted 14 June 2022
Available online 19 June 2022

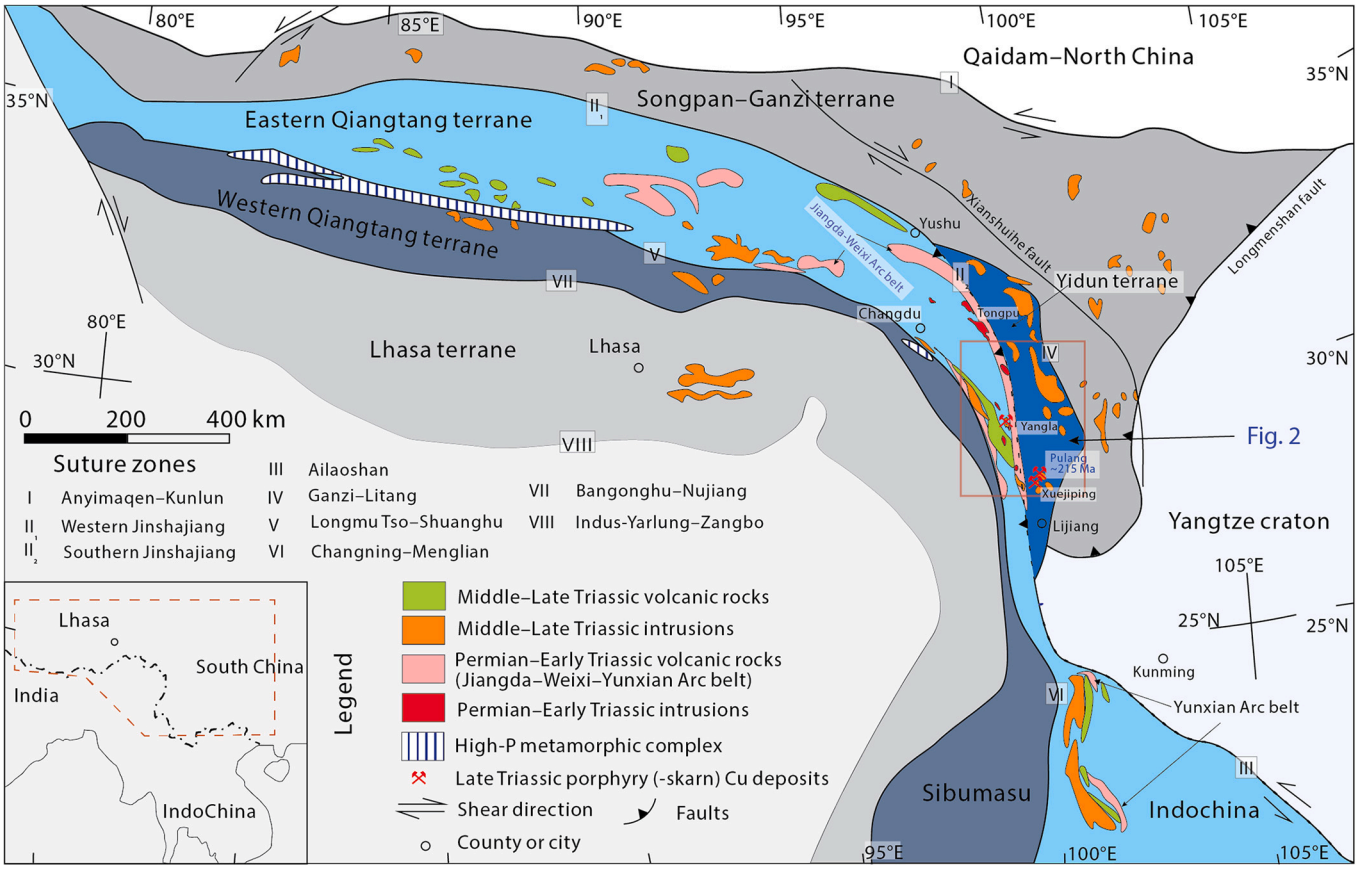

Fig. 1. Tectonic framework of the Sanjiang region, SW China showing the major terranes, suture zones, arc belts, Permian to Triassic igneous rocks, and locations of Late Triassic porphyry Cu deposits (Modified from Yang et al., 2014; Xu et al., 2015; Xin et al., 2018).

and volatile (H_2O-S-Cl) contents quantitatively in whole-rock samples. But the recent use of the accessory minerals zircon and apatite to assess porphyry Cu fertility has demonstrated that his technique can be widely applied (Lu et al., 2016; Zhu et al., 2018).

The Sanjiang region in SW China preserves a number of Late Carboniferous to Permian arc-related igneous rocks, associated with the subduction of the eastern Paleo-Tethyan Ocean (Metcalfe, 2021; Mo et al., 1993; Wang et al., 2018a; Xu et al., 2015; Yang et al., 2011), but coeval economic porphyry Cu deposits are rare (Richards, 2015b). Generally, porphyry Cu deposits (e.g., the giant Pulang Cu deposit) are found on the eastern margin of the Tethyan orogen, where they formed at ~216 Ma, significantly postdating closure of the Paleotethys (before ~230 Ma; Cao et al., 2019; Wang et al., 2018a; Wang et al., 2021). Furthermore, most studies focused on postcollisional Triassic granitoids, and petrogenesis of typical arc magmatism remains not well understood. In this contribution, we investigate the petrogenesis of Paleo-Tethyan arc igensous rocks and evaluate their magma fertility, with combination of whole-rock geochemistry and zircon and apatite compositions, and confirm that (1) the arc magmas were derived from the mixing of mantle and variable degree of crustal magmas, (2) they were indeed relatively reduced and therefore less fertile for porphyry Cu formation, and (3) compositions of zircon and apatite can be used as a tracer for porphyry Cu fertility.

2. Geological background

The Paleo-Tethyan Ocean opened along the northern margin of Gondwana during the early Late Paleozoic, and was then gradually consumed by subduction under the Eurasian continent prior to the mid-Mesozoic (Metcalfe, 2021; Wang et al., 2018a; Zhao et al., 2018; Zhu et al., 2013). The Sangjiang region forms the eastern segment of the Tethyan orogen, now on the southeastern margin of the Tibetan Plateau (Fig. 1). From west to east, the Sanjiang comprises the Western (South) Qiangtang, Eastern (North) Qiangtang–Indochina, Yidun, and Songpan–Ganzi terranes (Fig. 1). They are separated by three major NW-trending suture zones, which are from west to east the Longmu Tso-Shuanghu–Changning-Mengliang, Jinshajiang–Ailaoshan, and Ganzi–Litang (Fig. 1).

The Paleo-Tethys Ocean in the Sanjiang region can be divided into southern and northern branches (Zhao et al., 2018). It is generally accepted that the Longmu Tso-Shunaghu suture zone represents the closure of the main branch of the southern Paleo-Tethys Ocean, separating the Eastern Qiangtang terrane of Cathaysian affinity and the Gondwana-derived Western Qiangtang terrane (Li et al., 2006; Wang et al., 2018a; Yang et al., 2011; Zhu et al., 2013). The suture zone is characterized by Carboniferous and Permian ophiolites and an ~500-km long high-pressure metamorphic belt with an assemblage of Triassic eclogites and blueschists (Li et al., 2006; Zhang et al., 2011). To the south, the Longmu Tso-Shunaghu suture zone might connect with the Changning–Menglian suture (Deng et al., 2014; Metcalfe, 2021; Wang et al., 2018a). The eastward subduction (in present coordinates) of the main Paleo-Tethyan Ocean floor likely generated the Permian to Early Triassic S-trending Jiangda (Jomda)–Weixi–Yunxian arc belt in the Eastern Qiangtang terrane (Fig. 1; Yang et al., 2014; Xin et al., 2018). The southern Paleo-Tethyan ocean basin probably closed circa 250–230 Ma, leading to the collision of the Eastern Qiangtang with the Western Qiangtang, and the Sibumasu with the Indochina terranes (Wang et al., 2018a; Zhao et al., 2018).

To the east of the Longmu Tso–Shunaghu suture zone, the Jinshajiang (Jinsha) suture zone extends over 2000-km and can be divided

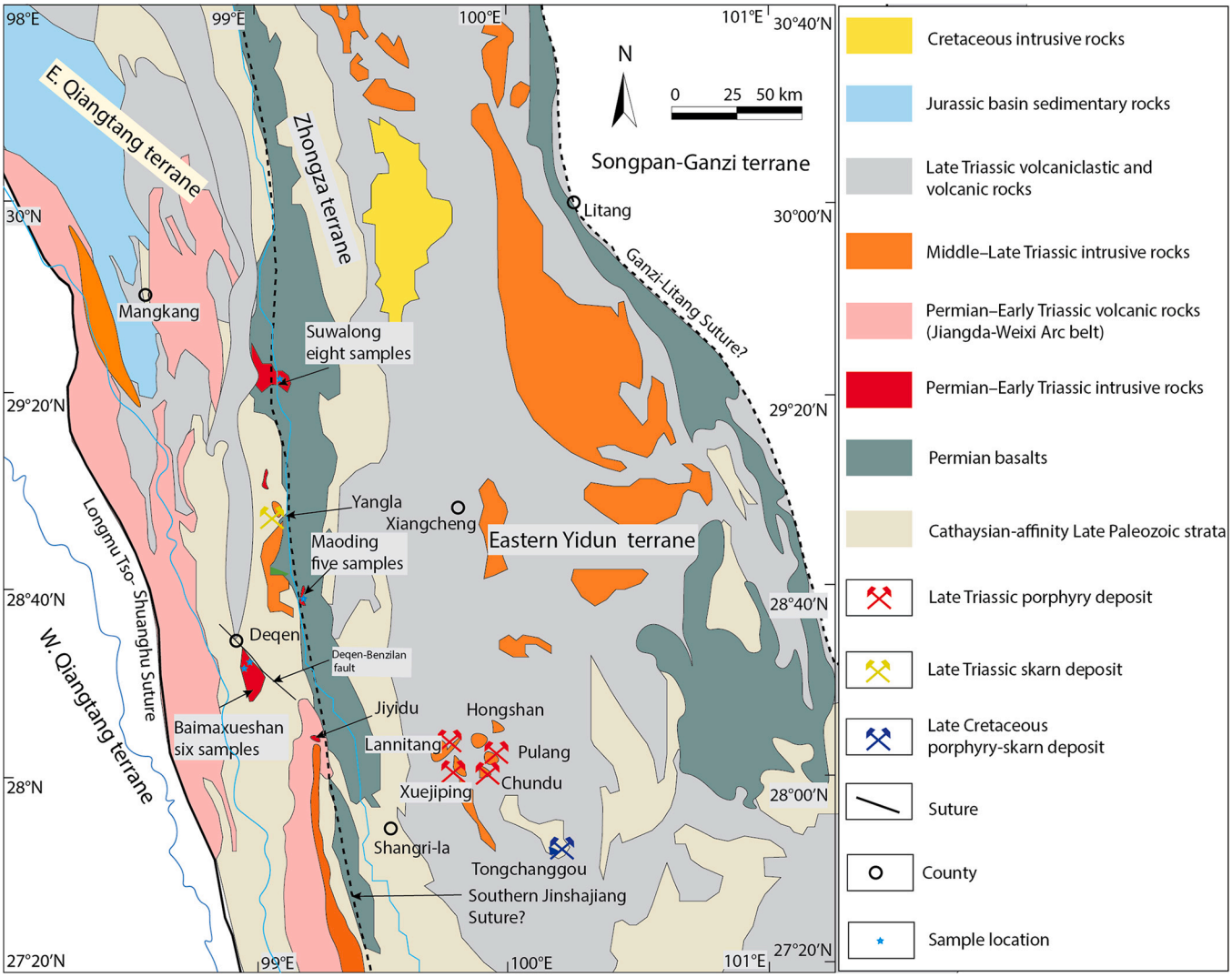

Fig. 2. Simplified geological map of the Eastern Qiangtang and Yidun terranes and the adjacent area showing the major suture zones of the Paleo-Tethyan Ocean (i.e., Longmu Tso–Shuanghu Suture), the granitic intrusions related to Paleo-Tethyan subduction (i.e., Maoding, Baimaxueshan, and Suwalong intrusions), and locations of Late Triassic porphyry Cu deposits (Modified from Yang et al., 2014). Abbreviations of blocks: E. Qiangtang = Eastern Qiangtang, W. Qiangtang = Western Qiangtang.

into two segments (Yang et al., 2014). The western segment defines the boundary between the Eastern Qiangtang and Songpan–Ganzi terranes, and probably records the closure of the Songpan–Ganzi Ocean or Mianlue Ocean, which was considered to be the northern branch of the Paleo-Tethyan Ocean (Zhao et al., 2018). It closed at 240–220 Ma, leading to the collision of the Eastern Qiangtang–Indochina–South China blocks with the North China and Qaidam blocks (Zhao et al., 2018). The southern segment of the Jinshajiang suture lies between the Eastern Qiangtang and western Yidun terranes (Figs. 1–2), but the nature of the suture remains a topic of debate. It might represent a remnant of the Jinshajiang Paleo-Tethyan Ocean marked by a series of ophiolitic fragments, and extends south to the Ailaoshan suture (Mo et al., 1993; Zi et al., 2012a) or a small back-arc/intra-arc basin formed by the east-dipping subduction of the main Paleo-Tethyan oceanic lithosphere (Wang et al., 2018a; Zhao et al., 2018).

The Jiangda–Weixi Arc belt is the focus of this study, defined by a ~400-km long series of NW-trending Permian to Lower Triassic volcaniclastic rocks in the southern part of the Eastern Qiangtang terrane (Fig. 1; Mo et al., 1993; Yang et al., 2011, 2014; Xin et al., 2018). It preserves the most representative Paleo-Tethyan arc igneous rocks in the Sanjiang region, probably associated with subduction of the main Paleo-Tethyan Ocean. The arc-related rocks comprise four lithological units with two suites of andesite, dacite, rhyolite, and minor basalt separated by two layers of limestone and shale (Xin et al., 2018; Yang et al., 2014). Several arc-related Permian to Early Triassic granitic batholiths are also found in the region (Wu et al., 2013; Yang et al., 2011). Late Triassic to Jurassic limestone and volcanic-siliciclastic rocks occur above an angular unconformity, which caps the Jiangda–Weixi Arc rocks (Li et al., 2006; Yang et al., 2014; Zhang et al., 2011). In addition, a number of south-trending Late Triassic post-orogenic granitoids (e.g., Jiaren, Dongdashan, and Ludian) occur along both sides of the Eastern Qiangtang terrane (Figs. 1–2; Zhu et al., 2011; Peng et al., 2015). No porphyry Cu deposits associated with Jiangda–Weixi arc magmatism have yet been found. The major porphyry mineralization in the Sanjiang region occurs at ~216 Ma within the Yidun terrane (Figs. 1–2), unrelated to the Paleo-Tethyan subduction (Wang et al., 2021). These include the Late Triassic Pulang (1625 Mt. @ 0.34% Cu and 0.18 g/t Au), Xuejiping (54 Mt. @ 0.53% Cu), and Lannitang (36 Mt. @ 0.5% Cu) Cu ± Au deposits, as well as a few porphyry Cu—Au prospects (Figs. 1 and 2; Deng et al., 2014; Cao et al., 2019; Yang and Cooke, 2019; Wang et al., 2021).

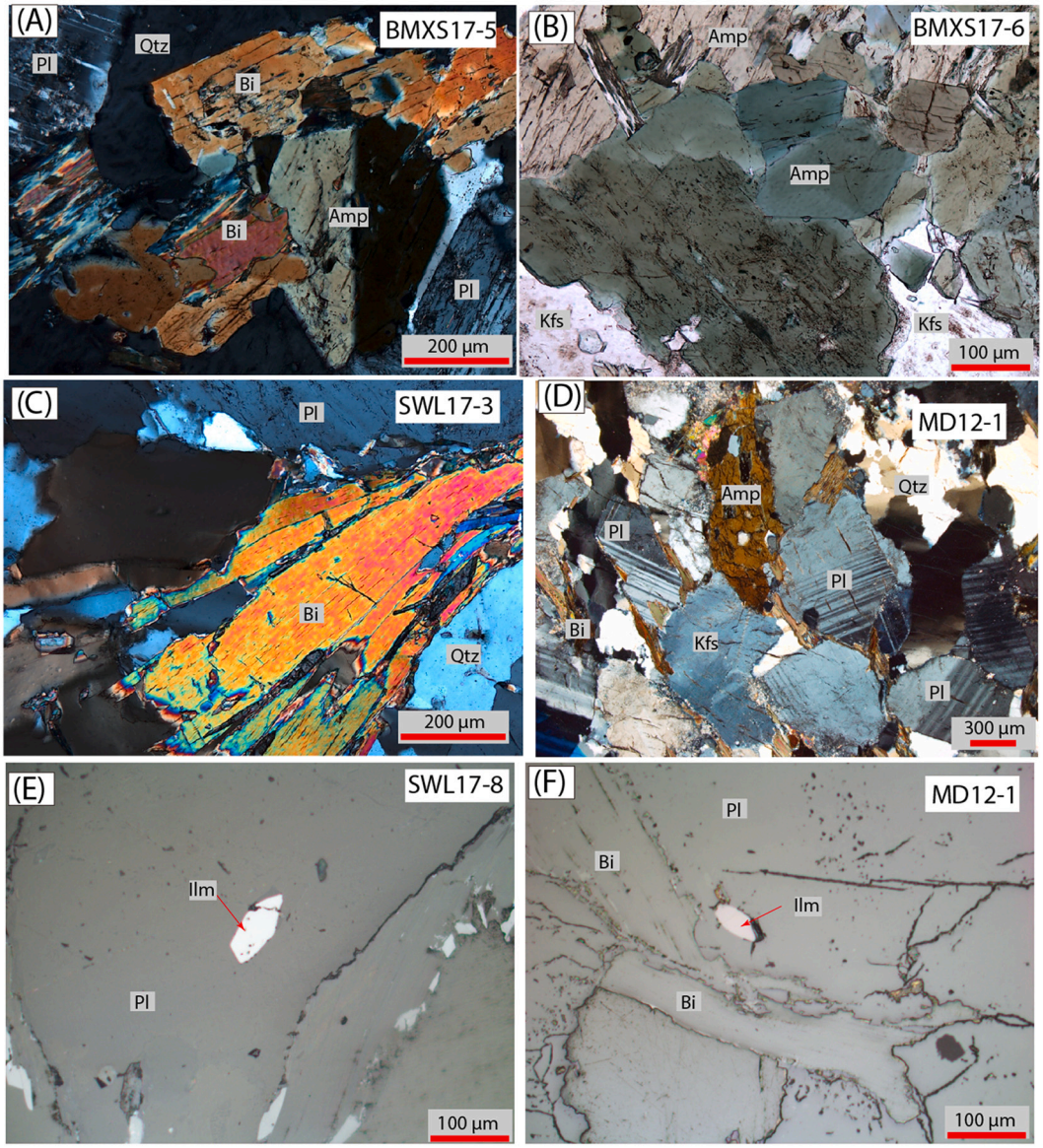

Fig. 3. Representative cross-polarized light photomicrographs showing (A–B) the Baimaxueshan granitoid (BMXS17–5, BMXS17–7), (C) the Suwalong (SWL17–3), and (C) Maoding (MD12–1) granodiorites, with coarse-grained amphibole and biotite; and backscattered electron images showing ilmenite inclusions within plagioclase or amphibole grains for (E) Suwalong (SWL17–8), and (F) Maoding (MD12–1) granodiorites. Abbreviations: Amp = amphibole, Bi = biotite, Ilm = ilmenite, Kfs = K-feldspar, Pl = plagioclase, Qtz = quartz.

3. Samples and analytical methods

A series of Permian to Early Triassic granitoids have been emplaced in the Jiangda–Weixi Arc belt, including, from north to south, the Tongpu, Suwalong, Maoding, Baimaxueshan, and Jiyidu plutons (Jian et al., 2003; Wu et al., 2013; Yang et al., 2011; Zi et al., 2012b). Samples were collected from the Baimaxueshan, Suwalong, and Maoding intrusions (Fig. 2). The Baimaxueshan pluton is located ~30 km south of Deqin county, Yunan province, with an outcrop area of ~135 km^2. It intruded the Upper Permian schists and marbles (Zi et al., 2012a), and is mainly composed of medium-grained granodiorite, with 35–40 vol% plagioclase, 20–25 vol% K-feldspar, 25 vol% quartz, 5–10 vol% amphibole, and 5 vol% biotite (Fig. 3A–B). Zircon U—Pb dating yielded a relatively large range of ages between 255 Ma and 239 Ma, consistent with the Paleo-Tethyan subduction or the early stage of collision (He et al., 2018; Jian et al., 2003; Zi et al., 2012a).

The Suwalong intrusion is located on the east bank of the Jinshajiang River, ~70 km south of Batang county, Sichuan province, with an outcrop area of ~30 km^2 (Fig. 2). It intruded Devonian to Carboniferous schist and marble, and is cut by the S-trending Suwalong–Wubalong fault (SCBGMR, 1977). The intrusive rocks range from biotite granite to granodiorite, with medium- to fine-grained textures, and are composed of K-feldspar (40–45 vol%), plagioclase (25 vol%), quartz (20–25 vol%), biotite (5 vol%), and amphibole (5 vol%; Fig. 3C; SCBGMR, 1977).

The Maoding pluton (~1 km^2) is located ~2 km southeast of the Late Triassic Jiaren batholith (~150 km^2), and is crosscut by the Jinshajiang River (Fig. 2; Zhu et al., 2011). It is a fine-grained granodiorite composed of plagioclase (40–45 vol%), K-feldspar (20 vol%), quartz (20–25 vol%), amphibole (5 vol%), and biotite (5 vol%, locally showing gneissic structure; Fig. 3D), intruding the the Devonian carbonate and sandstone sequences. All the three granitoids above host ilmenite grains, typical of ilmenite-series granite (Figs. 3E–F).

Twenty-one samples from the Baimaxueshan, Suwalong, and Maoding granitoids were collected from outcrop. Detailed descriptions and locations are listed in digital Appendix Table A1. Eighteen fresh samples from the three granitoids plutons were selected for whole-rock

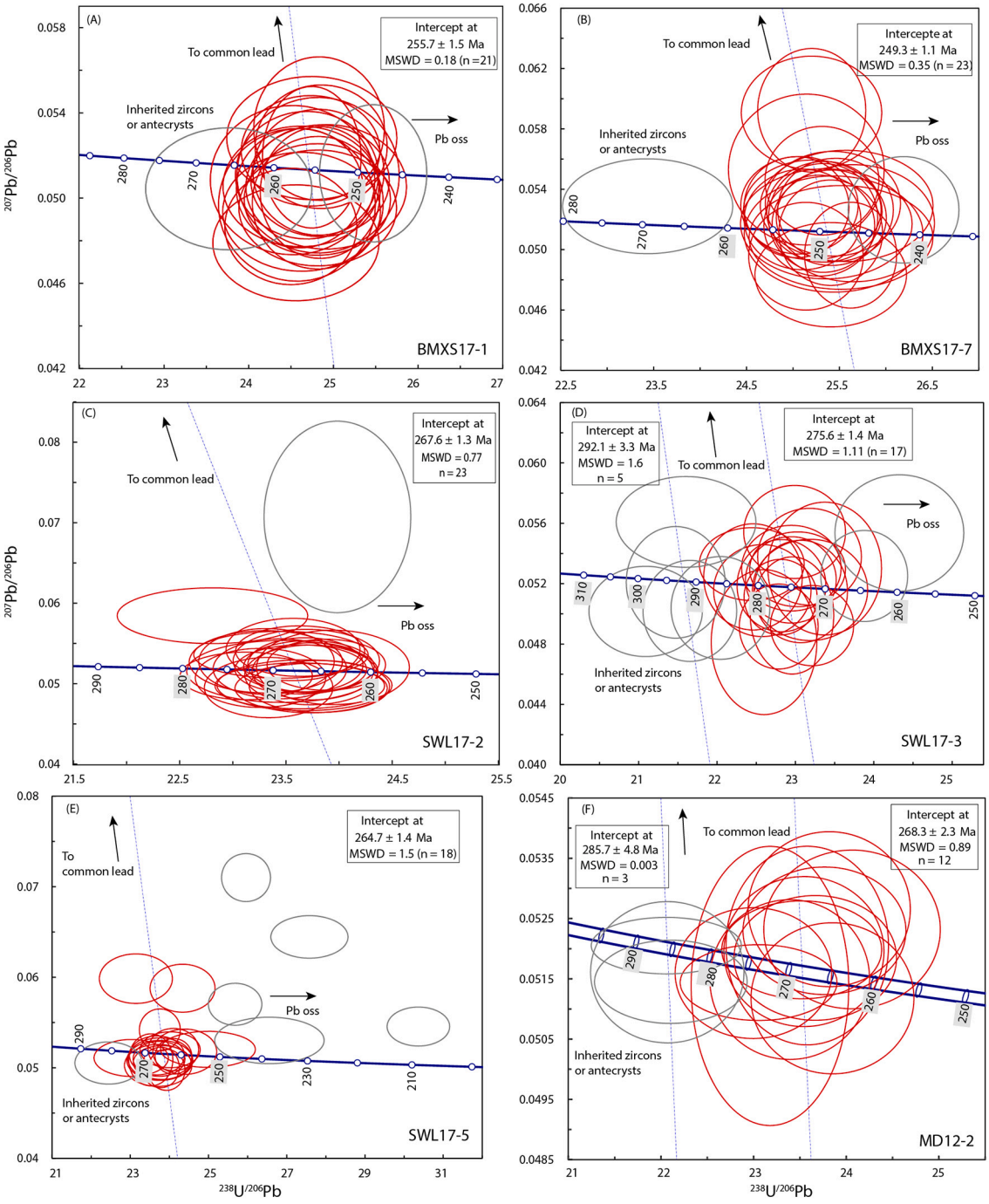

Fig. 4. Zircon U—Pb Tera-Wasserburg concordia diagrams for the Baimaxueshan, Suwalong, and Maoding granitoids (Tera and Wasserburg, 1972). Samples (A) BMXS17–1, (B) BMXS17–7, (C) SWL17–2, (D) SWL17–3, (E) SWL17–5, and (F) MD12–2. Gray ellipses are analyses excluded from the age calculation (see text for details). Uncertainty ellipses and calculated ages are shown at 2σ.

geochemical and electron microprobe (apatite) analyses, with six of them (three from Suwalong, one from Maoding, and two from Baimaxueshan) also prepared for zircon U—Pb dating and trace element measurements. One sample from the Maoding intrusion was used for zircon Hf—O as well. Detailed analytical methods can be found in Appendix 1.

4. Results

4.1. Zircon U—Pb isotopic results

Zircon U—Pb data for the Baimaxueshan and Suwalong granitoids are presented in digital Appendix Tables A2, and A3 for the Maoding granitoid. All the results are also illustrated in Fig. 4. Samples BMXS17–1 and BMXS17–7 were obtained from the Baimaxueshan pluton. Analyzed zircon grains from the two samples both show tightly clustered ages, mostly with low common lead contents (Figs. 4A–B). Sample BMXS17–1 yielded an intercept age of 255.7 ± 1.5 Ma (MSWD

Table 1
Major and trace element compositions of the Baimaxueshan, Suwalong, and Maoding intrusions and Pulang porphyry.

	Bamaxueshan intrusion						Suwalong intrusion							Maoding intrusion			
SAMPLE #	BMXS17–1	BMXS17–3	BMXS17–4	BMXS17–5	BMXS17–6	BMXS17–7	SWL17–1	SWL17–3	SWL17–4	SWL17–5	SWL17–6	SWL17–7	SWL17–8	MD12–1	MD12–1-0	MD12–3	MD12–3-0
Weight %																	
SiO_2	64.70	63.00	63.12	63.93	63.19	61.78	68.22	68.64	69.33	73.15	68.81	61.24	69.25	67.00	68.18	69.42	64.70
Al_2O_3	15.00	15.38	15.24	15.50	15.07	16.36	15.60	15.82	15.48	14.71	16.22	19.06	15.76	16.77	16.50	15.59	18.01
CaO	4.25	4.51	4.57	4.54	4.53	5.82	4.06	3.69	3.62	2.52	4.15	6.55	3.61	4.22	3.72	3.53	4.93
Fe_2O_3(T)	4.59	5.06	4.97	5.10	4.88	6.40	3.73	2.88	3.11	1.94	2.64	3.80	3.06	3.10	2.50	2.63	3.32
K_2O	3.50	3.19	3.00	3.39	3.25	2.44	0.90	1.61	1.19	1.28	1.15	0.94	1.54	0.96	1.32	0.91	0.98
MgO	2.97	3.35	3.23	3.25	3.13	2.66	1.90	1.35	1.38	0.58	1.19	2.20	1.35	1.34	1.15	1.09	1.71
MnO	0.07	0.08	0.08	0.08	0.08	0.10	0.06	0.05	0.05	0.05	0.05	0.06	0.06	0.04	0.04	0.03	0.06
Na_2O	2.67	2.66	2.62	2.71	2.68	2.04	4.38	3.85	4.04	4.78	4.30	4.56	4.08	4.82	4.73	4.43	4.82
P_2O_5	0.20	0.23	0.22	0.22	0.20	0.13	0.14	0.08	0.07	0.05	0.09	0.16	0.08	0.10	0.09	0.03	0.14
TiO_2	0.50	0.57	0.56	0.56	0.54	0.72	0.53	0.35	0.38	0.20	0.37	0.57	0.37	0.32	0.25	0.25	0.28
LOI	1.13	1.68	1.97	1.02	1.73	1.68	0.75	1.10	0.82	0.65	0.69	0.94	1.09	0.47	0.55	0.57	0.67
Total	99.58	99.71	99.58	100.30	99.28	100.13	100.27	99.42	99.47	99.91	99.66	100.08	100.25	99.14	99.03	98.48	99.62
Parts per million																	
Cr	108	121	110	116	83.4	34.0	20.2	25.9	17.8	15.0	18.5	32.3	17.1	39.8	23.1	25.1	33.1
Co	12.5	14.0	13.7	14.0	13.5	12.3	8.66	6.12	6.55	2.96	5.35	11.1	6.48	7.65	5.65	5.36	8.10
Ni	28.3	32.5	31.0	30.0	25.5	6.15	6.79	6.89	6.31	1.63	4.24	11.7	7.12	38.4	16.7	15.2	21.8
Rb	151	134	136	151	133	98.4	30.2	63.0	47.9	55.4	43.6	31.8	59.4	34.0	50.2	31.8	30.5
Sr	419	468	453	459	437	239	256	262	250	183	283	368	260	385	331	337	427
Y	19.6	22.9	22.0	21.0	19.5	28.2	11.10	6.08	5.68	9.56	8.17	12.87	7.20	6.73	4.53	7.44	5.24
Nb	11.0	12.2	12.4	11.9	10.7	9.9	3.45	3.89	3.25	5.62	3.24	3.50	3.49	2.83	3.35	3.48	3.22
Ta	1.11	1.26	1.50	1.18	1.12	0.85	0.29	0.35	0.19	0.56	0.22	0.30	0.27	0.16	0.28	0.38	0.15
Ba	719	688	605	711	611	495	178	310	279	190	191	187	305	206	220	243	188
Hf	4.22	4.86	4.68	4.95	4.40	3.09	3.92	2.57	2.75	2.89	2.51	3.36	2.64	2.59	2.41	2.69	1.81
Zr	144	183	171	185	154	104	152	103	113	85	105	143	100	115	102	103	90
La	43.5	58.6	41.3	37.0	41.2	32.7	9.2	13.6	11.6	16.4	9.9	6.6	13.7	5.07	9.73	9.24	4.50
Ce	82.5	107.0	80.0	71.6	79.8	65.4	19.5	27.1	22.7	30.9	19.7	14.3	26.2	11.0	18.3	17.8	8.9
Pr	8.89	11.10	8.64	8.03	8.64	7.03	2.23	2.82	2.51	3.35	2.25	1.90	2.92	1.29	1.85	1.92	1.05
Nd	32.9	40.4	32.8	31.4	31.8	27.0	9.23	10.60	9.54	12.50	9.03	8.45	11.40	5.71	6.72	7.29	4.72
Sm	5.73	6.64	5.96	5.89	5.49	5.20	2.13	1.60	1.60	2.69	1.99	2.28	1.96	1.44	1.32	1.59	1.15
Eu	1.44	1.52	1.38	1.42	1.35	1.14	0.58	0.66	0.66	0.56	0.64	0.82	0.64	0.58	0.54	0.59	0.66
Gd	4.87	5.58	5.16	5.06	5.03	5.09	2.01	1.42	1.43	2.35	1.82	2.31	1.83	1.22	1.09	1.34	1.09
Tb	0.64	0.75	0.71	0.69	0.64	0.79	0.31	0.18	0.19	0.35	0.26	0.38	0.22	0.23	0.16	0.24	0.17
Dy	3.26	3.85	3.74	3.60	3.33	4.95	1.83	1.00	0.93	1.79	1.49	2.27	1.24	1.21	0.81	1.18	0.92
Ho	0.64	0.75	0.74	0.71	0.64	0.96	0.34	0.20	0.17	0.31	0.26	0.45	0.24	0.23	0.17	0.26	0.18
Er	1.77	2.14	2.08	1.92	1.90	2.80	1.11	0.57	0.52	0.88	0.83	1.22	0.64	0.65	0.44	0.72	0.51
Tm	0.25	0.28	0.27	0.25	0.27	0.40	0.15	0.09	0.07	0.12	0.10	0.18	0.09	0.09	0.06	0.12	0.08
Yb	1.55	1.85	1.88	1.69	1.77	2.59	1.06	0.60	0.55	0.79	0.67	1.21	0.66	0.65	0.44	0.78	0.49
Lu	0.25	0.28	0.30	0.27	0.25	0.36	0.15	0.08	0.08	0.12	0.10	0.16	0.10	0.08	0.07	0.12	0.08
U	6.56	4.75	7.95	4.48	4.40	1.30	0.69	0.81	0.63	1.86	0.59	1.57	0.66	0.43	0.48	1.09	0.42
Th	23.2	24.9	17.4	16.0	17.5	13.7	2.82	4.35	3.47	8.09	2.99	2.25	4.11	1.18	2.31	3.57	0.61
Pb	35.5	29.9	33.3	32.2	34.8	23.4	6.95	8.78	7.16	18.00	7.35	8.96	8.15	6.41	8.54	10.50	5.61

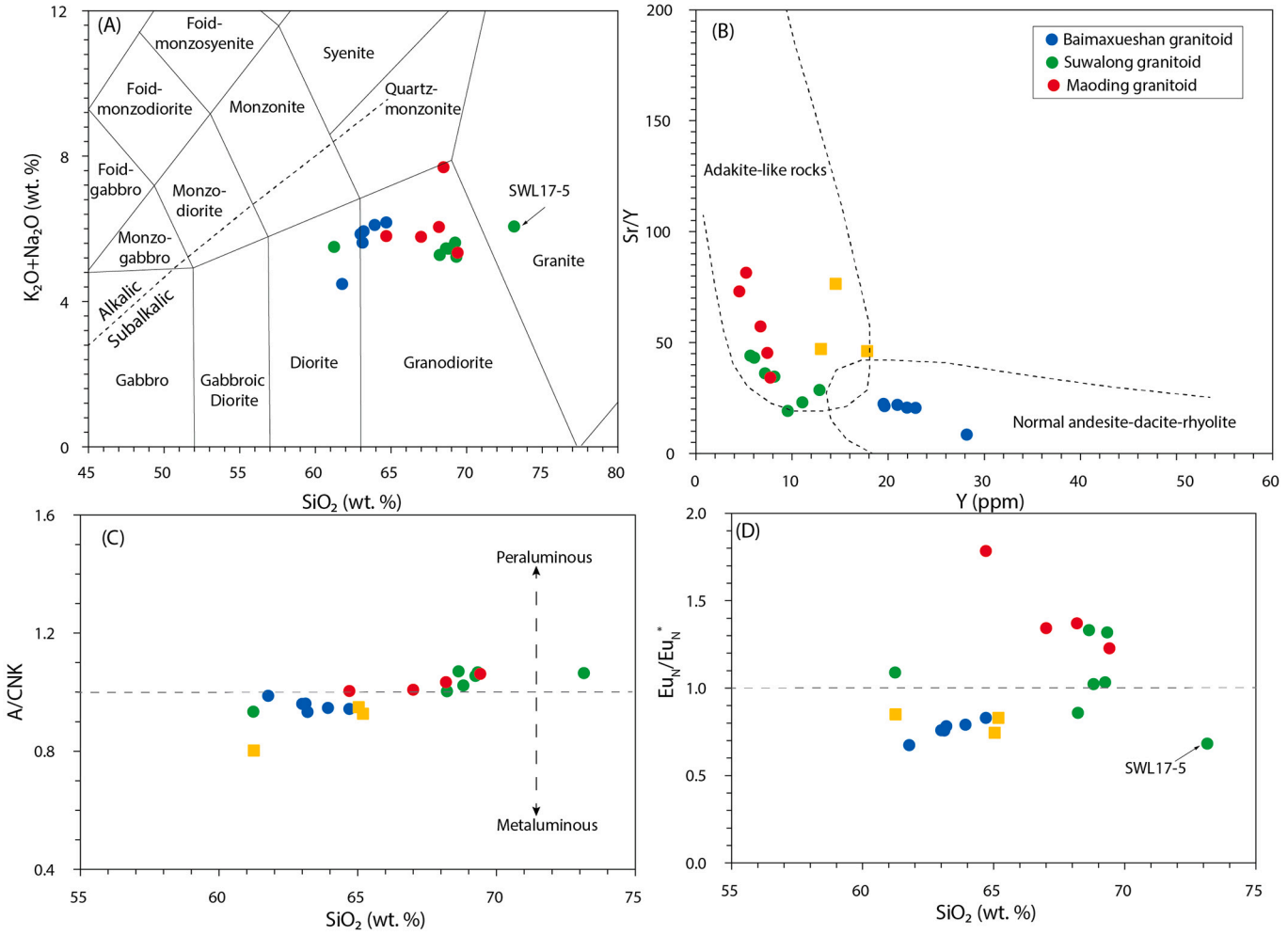

Fig. 5. (A) Total alkali-silica diagram (Middlemost, 1994), (B) Sr/Y ratios vs. Y, (C) SiO_2 vs. A/CNK [molar $Al_2O_3/(CaO + Na_2O + K_2O)$], and (D) SiO_2 vs. Eu_N/Eu_N^* for the Baimaxueshan, Suwalong, and Maoding granitoids. Normalizing values from Sun and McDonough (1989).

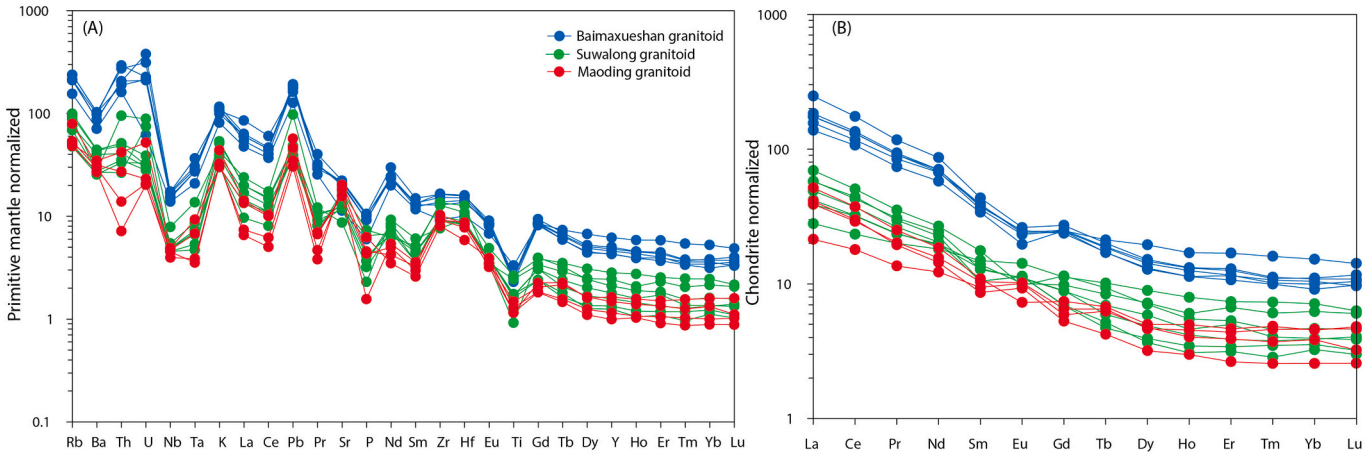

Fig. 6. (A) Primitive mantle-normalized trace element and (B) chondrite-normalized rare earth element diagrams for the Baimaxueshan, Suwalong, and Maoding granitoids. The normalizing values for primitive mantle and chondrite are from Sun and McDonough (1989).

= 0.18; Fig. 4A) based on 21 of 25 grains, consistent with weighted mean $^{206}Pb/^{238}U$ ages of 255.5 ± 1.5 Ma (MSWD = 0.13). The four excluded grains include two with much older ages (apparent $^{206}Pb/^{238}U$ ages = 329 ± 7.2 Ma and 1075 ± 34.3 Ma, respectively; digital App. Table A2), and one grain having slightly older $^{206}Pb/^{238}U$ age of 266 ± 8.8 Ma, indicative of xenocrysts or antecrysts (Fig. 4B). The other zircon grain yielded a slightly younger $^{206}Pb/^{238}U$ age (248 ± 5.0 Ma), probably explained by lead loss (Fig. 4B). Twenty-five zircon grains from sample BMXS17–7 were selected for analyses, and one xenocrystic zircon grain was found, with a $^{206}Pb/^{238}U$ age of 269.4 ± 8.4 Ma

Table 2
Whole-rock Nd—Sr Isotopic Results for the Baimaxueshan, Suwalong, and Maoding intrusions in the Jiangda–Weixi belt[1].

Sample no.	Rb (μg/g)	Sr (μg/g)	$^{87}Sr/^{86}Sr$	± σ	Sm (μg/g)	Nd (μg/g)	$^{143}Nd/^{144}Nd$	± 2σ	$(^{143}Nd/^{144}Nd)t$	$(^{87}Sr/^{86}Sr)t$	ε_{Nd} (t = 250 Ma)	T_{DM1} (Ma)	T_{DM2} (Ma)
Baimaxueshan intrusion													
BMXS17–1	151	419	0.713422	0.000004	5.73	32.9	0.512147	0.000002	0.511975	0.7097	−6.7	1411	1569
BMXS17–7	98.4	239	0.716986	0.000005	5.2	27	0.511961	0.000002	0.511770	0.7128	−10.7	1862	1889
Suwalong intrusion													
SWL17–1	30.2	256	0.705561	0.000004	2.13	9.23	0.512667	0.000003	0.512439	0.7043	2.4	994	820
SWL17–3	63	262	0.707474	0.000004	1.6	10.6	0.512546	0.000002	0.512396	0.7050	1.6	754	905
SWL17–5	55.4	183	0.708723	0.000005	2.69	12.5	0.512560	0.000004	0.512347	0.7056	0.6	1078	970
SWL17–5 (repetition)	55.4	183	0.70878	0.000005	2.69	12.5	0.512549	0.000003	0.512336	0.7057	0.4	1098	988
SWL17–7	31.8	368	0.70571	0.000004	2.28	8.45	0.512660	0.000004	0.512393	0.7048	1.5	1479	884
SWL17–8	59.4	260	0.707212	0.000005	1.96	11.4	0.512564	0.000002	0.512394	0.7049	1.5	816	905
Maoding intrusion													
MD12–1	34	385	0.705191	0.000007	1.44	5.71	0.512721	0.000009	0.512472	0.7043	3.0	1071	763
MD12–1-0	50.2	331	0.705836	0.000006	1.32	6.72	0.512599	0.000005	0.512405	0.7043	1.7	887	882
MD12–3	31.8	337	0.705593	0.000004	1.59	7.29	0.512624	0.000007	0.512408	0.7046	1.8	982	872
MD12–3-0	30.5	427	0.704961	0.000009	1.15	4.72	0.512682	0.000007	0.512441	0.7042	2.4	1077	814

Notes: [1]Rb, Sr, Sm, and Nd concentrations from Table 1; $T_{DM1} = (1/\lambda) \times Ln[((^{143}Nd/^{144}Nd)_{sample}-(^{143}Nd/^{144}Nd)_{DM})/((^{147}Sm/^{144}Nd)_{sample}-(^{147}Sm/^{144}Nd)_{DM} + 1)]$ and $T_{DM2} = T_{DM1} - (T_{DM1} - t) \times ((f_{cc} - f_s)/(f_{cc} - f_{DM}))$ calculation for T_{DM2} following assuming of Keto and Jacobsen (1987) where $f_{cc} = -0.4$, $f_{DM} = 0.0859$. See Appendix 1 for the $^{143}Nd/^{144}Nd$ and $^{147}Sm/^{144}Nd$ values of present day chondrite and depleted mantle.

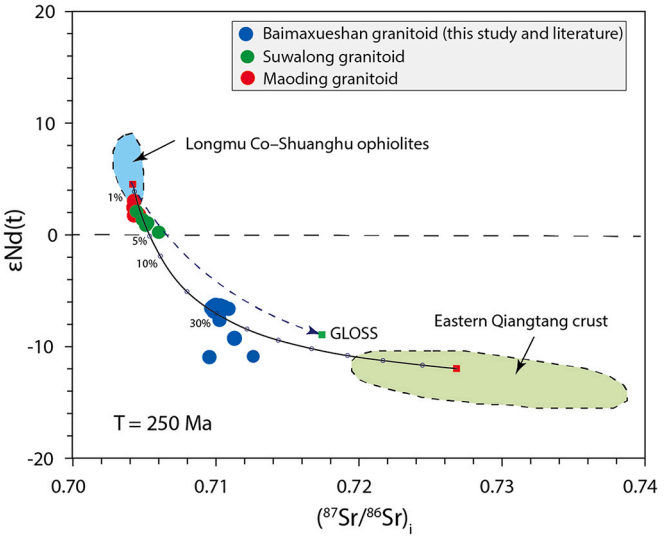

Fig. 7. $\varepsilon_{Nd}(t)$ vs. initial $^{87}Sr/^{86}Sr$ ratios for the Baimaxueshan, Suwalong, and Maoding granitoids at $t = 250$ Ma. Data from the Baimaxueshan from Zi et al. (2012a), He et al. (2018), and this study. The mantle field represented by the Longmu Co–Shuanghu ophiolites after Zhai et al. (2019); the Eastern Qiangtang curst field represented by granite after Peng et al. (2015); global subducting sediment (GLOSS) after Plank and Langmuir (1998). The parameters used in the mixing calculations: mantle-derived melt, 164 ppm Sr, 6.69 ppm Nd, initial $^{87}Sr/^{86}Sr = 0.7041$, $\varepsilon_{Nd}(t) = 4.6$; crustal-derived melt, 131 ppm Sr, 39.1 ppm Nd, initial $^{87}Sr/^{86}Sr = 0.7275$, $\varepsilon_{Nd}(t) = -12.1$.

(digital App. Table A2). Another crystal with $^{206}Pb/^{238}U$ age of 241.6 ± 4.4 Ma might be caused by lead loss (Fig. 4B). The remaining 23 zircon grains intersected the concordia line at 249.3 ± 1.1 Ma (MSWD = 0.35; Fig. 4B), in good agreement with the weighted mean $^{206}Pb/^{238}U$ age of 249.7 ± 1.1 Ma (MSWD = 0.41). These intercept ages are considered to be the emplacement ages for the Baimaxueshan intrusion. They are consistent with recently published zircon U—Pb ages (He et al., 2018; Zi et al., 2012a), and collectively defined a magmatic duration of ~6 m.y. from 255.7 ± 1.5 Ma to 249.3 ± 1.1 Ma for Baimaxueshan.

Samples SWL17–2, SWL17–3, and SWL17–5 were collected from the Suwalong granitoid. For sample SWL17–2, excluding one xenocryst with an older $^{206}Pb/^{238}U$ age of 545 ± 38.8 Ma (digital App. Table A2) and one grain with a younger discordant age due to lead loss (apparent $^{206}Pb/^{238}U$ age = 263.3 ± 6.1 Ma), the remaining 23 crystals yielded a homogeneous age population with low common lead contents (Fig. 4C). Regression of this population yielded an intercept age of 267.6 ± 1.3 Ma (MSWD = 0.77; Fig. 4C), similar to the weighted mean $^{206}Pb/^{238}U$ age (267.8 ± 1.3 Ma; MSWD = 0.83). Twenty-five crystals from sample SWL17–3 were selected for analyses with one xenocryst yielding an older $^{206}Pb/^{238}U$ age of 426.4 ± 23.8 Ma (digital App. Table A2). Twenty-two grains show two age groups on a $^{206}Pb/^{238}U$ age histogram and the concordia diagram (Fig. 4D). One group intercepts the concordia line at 292.1 ± 3.3 Ma (MSWD = 1.6; $n = 5$), whereas a younger group yielded an intercept age of 275.6 ± 1.4 Ma (MSWD = 1.11; $n = 17$). The young age might best represent the emplacement age of the rock, consistent with their weighted mean $^{206}Pb/^{238}U$ age (275.5 ± 1.4 Ma, MSWD = 1.04). The older group is likely of antecrystic or inherited origin. The remaining two crystals plotted to the right of the younger group reflecting lead loss (Fig. 4D). Sample SWL17–5 has a relatively scattered distribution of individual zircon spot ages, probably caused by an antecryst or inherited zircon grain ($^{206}Pb/^{238}U$ age = 281.0 ± 8.6 Ma), and six young crystals with lead loss (digital App. Table A2; Fig. 4E). The young zircon grains show relatively high common lead contents, with variable $^{206}Pb/^{238}U$ ages from 246 to 115 Ma (digital App. Table A2). The remaining 18 crystals yielded low amounts of common lead and intercept the concordia line at 264.7 ± 1.4 Ma (MSWD = 18; Fig. 4E), in good agreement with the weighted mean $^{206}Pb/^{238}U$ age of 264.6 ± 1.4 Ma (MSWD = 1.4). The intercept ages for the Suwalong intrusion are interpreted to be its crystallization ages, and define a ~ 11-m.y. span of magmatism from 275.6 ± 1.4 Ma to 264.7 ± 1.4 Ma.

Sample MD12–2 was obtained from the Maoding intrusion. Fifteen analyzed zircon grains show two age groups, both with low common lead contents (digital App. Table A3; Figs. 4F). One group of three crystals yielded an intercept age of 285.7 ± 4.8 Ma (MSWD = 0.003), and the other group intercepts the Concordia line at 268.3 ± 2.3 Ma (MSWD = 0.89; Fig. 4F). The older group could represent antecrysts or

Table 3
In situ zircon Hf—O isotope compostions for the Maoding intrusion.[1]

Spot no.	$^{176}Hf/^{177}Hf$	1σ	$^{176}Lu/^{177}Hf$	1σ	$^{176}Yb/^{177}Hf$	1σ	Hf (μg/g)	Yb (μg/g)	Lu (μg/g)	Age (Ma)	$\varepsilon_{Hf}(t)$	1σ	T_{DM1} (Ma)	$\varepsilon_{Hf}(0)$	1σ	$f_{Lu/Hf}$	$\delta^{18}O$ (‰)	2σ
MD12–2@1	0.283046	0.000022	0.000772	0.000022	0.021484	0.000639	10,126	344	56.1	268	15.5	1.0	290	9.7	0.9	−1.0	n/a	n/a
MD12–2@2	0.283035	0.000019	0.001115	0.000014	0.031687	0.000689	11,281	577	92.7	268	15.0	0.9	308	9.3	0.9	−1.0	6.9	0.4
MD12–2@3	0.283056	0.000020	0.000985	0.000014	0.026424	0.000267	8474	356	60.4	268	15.8	0.9	278	10.0	0.9	−1.0	6.5	0.4
MD12–2@4	0.283126	0.000025	0.001415	0.000120	0.038417	0.003528	12,844	744	126.1	268	18.2	1.1	180	12.5	1.0	−1.0	6.5	0.4
MD12–2@5	0.283066	0.000018	0.001065	0.000007	0.026488	0.000162	13,855	580	107.0	268	16.1	0.8	264	10.4	0.8	−1.0	5.9	0.4
MD12–2@6	0.283045	0.000019	0.001048	0.000041	0.026824	0.001152	14,632	631	112.8	268	15.4	0.9	293	9.6	0.8	−1.0	5.9	0.4
MD12–2@7	0.283057	0.000018	0.001405	0.000027	0.035233	0.000845	12,568	722	131.6	285	16.1	0.8	279	10.1	0.8	−1.0	6.8	0.4
MD12–2@8	0.283128	0.000020	0.001273	0.000007	0.035528	0.000223	10,618	601	99.1	285	18.6	0.9	176	12.6	0.9	−1.0	6.1	0.4
MD12–2@9	0.283097	0.000022	0.001677	0.000052	0.047133	0.001319	10,437	758	123.4	268	17.1	1.0	223	11.5	0.9	−0.9	6.0	0.4
MD12–2@10	0.283121	0.000025	0.001154	0.000013	0.032818	0.000397	8444	445	70.9	285	18.4	1.0	185	12.4	1.0	−1.0	5.6	0.4
MD12–2@11	0.283093	0.000028	0.001281	0.000007	0.032619	0.000342	7705	404	72.2	268	17.0	1.1	226	11.3	1.1	−1.0	5.7	0.4
MD12–2@12	0.283062	0.000024	0.000886	0.000029	0.023155	0.000590	11,425	408	71.2	268	16.0	1.0	267	10.3	1.0	−1.0	6.4	0.4
MD12–2@13	0.283076	0.000027	0.001096	0.000035	0.028161	0.000863	9525	414	73.7	268	16.4	1.1	250	10.7	1.1	−1.0	6.4	0.4
MD12–2@14	0.283103	0.000023	0.001216	0.000007	0.032664	0.000353	10,611	554	94.3	268	17.4	1.0	211	11.7	0.9	−1.0	6.2	0.4
MD12–2@15	0.283102	0.000020	0.001088	0.000020	0.028714	0.000753	10,259	479	82.8	268	17.4	0.9	212	11.7	0.9	−1.0	n/a	n/a
MD12–2@16	0.283028	0.000019	0.000640	0.000003	0.016820	0.000143	11,952	322	55.8	268	14.9	0.9	313	9.1	0.8	−1.0	n/a	n/a
MD12–2@17	0.283031	0.000018	0.001162	0.000005	0.029753	0.000098	11,920	564	100.9	268	14.8	0.8	315	9.1	0.8	−1.0	7.9	0.4
MD12–2@18	0.283013	0.000020	0.000759	0.000005	0.019045	0.000132	13,000	396	72.3	268	14.3	0.9	337	8.5	0.9	−1.0	5.9	0.4

[1] Age results see Table A3; "n/a" = no data; $T_{DM1} = (1/\lambda) \times Ln[((^{176}Hf/^{177}Hf)_{sample}-(^{176}Hf/^{177}Hf)_{DM})/((^{176}Lu/^{177}Hf)_{sample}-(^{176}Lu/^{177}Hf)_{DM}+1)]$. See Appendix 1 for the $^{177}Hf/^{176}Hf$ and $^{177}Lu/^{176}Hf$ values of present day chondrite and depleted mantle.

inherited zircon grains. The young age might best represent the crystallization age of the intrusion, consistent with the weighted mean $^{206}Pb/^{238}U$ age of 268.2 ± 2.3 Ma (MSWD = 0.88).

In summary, the three granite intrusions were emplaced between ~275–249 Ma.

4.2. Whole-rock major and trace elements

Whole-rock geochemical compositions for 20 samples of the three Permian to Early Triassic granitoids are reported in Table 1 and illustrated on Figs. 5–6. The Baimaixueshan, Suwalong, and Maoding intrusions are mostly felsic (SiO_2 = 61.78–73.15 wt%), calc-alkaline to high-K calc-alkaline ($K_2O + Na_2O$ = 4.48–6.17 wt%) and have compositions from diorite to granodiorite (except SWL17–5 plotted in the field of granite; Fig. 5A). They are metaluminous to slightly peraluminous, with A/CNK ratios [molar $Al_2O_3/(CaO + Na_2O + K_2O)$] from 0.93 to 1.07 (Fig. 5C). On primitive mantle-normalized trace element and chondrite-normalized rare earth element (REE) diagrams, all the granitoid rocks show similar patterns (Fig. 6), characterized by high contents of large-ion-lithophile elements (LILEs: Ba, Rb, U, Th, K) and light rare earth elements (LREE), with low concentrations of high-field-strength elements (HFSEs: Nb, Ta, Ti, Zr, Hf). Middle to heavy rare earth elements (MREE, HREE; La/Yb = 17.9 ± 7.6, n = 17) are relatively depleted, with flat- to listric-shaped patterns (Gd/Yb = 2.5 ± 0.5, n = 17). All the samples have relatively high but variable Sr/Y ratios (35 ± 20, n = 17; Fig. 5B), with slightly negative to positive Eu anomalies ($Eu_N/Eu_N^* = Eu_N/(Sm_N \times Gd_N)^{0.5}$ = 1.04 ± 0.3, n = 17; Fig. 5D).

4.3. Whole-rock Sr—Nd isotopes

New Sr—Nd isotope data for the Baimaxueshan, Suwalong, and Maoding intrusions are presented in Table 2 and Fig. 7. Two samples from the Baimaxueshan granite have initial Sr isotope ratios of 0.7097 and 0.7128, coupled with negative $\varepsilon_{Nd}(t)$ values of −6.7 and − 10.7. The Suwalong intrusion has low initial Sr isotope ratios from 0.7043 to 0.7057 [$(^{87}Sr/^{86}Sr)_t$ = 0.7049 ± 0.0005, n = 5; t = 250 Ma), with positive $\varepsilon_{Nd}(t)$ values of +0.4 − +2.4 (1.5 ± 0.6, n = 5). The Maoding has a narrow range of initial Sr isotope ratios from 0.7043 to 0.7048 [$(^{87}Sr/^{86}Sr)_t$ = 0.7045 ± 0.0002, n = 4; t = 250 Ma] and $\varepsilon_{Nd}(t)$ values from 1.4 to 2.8 (2.3 ± 0.6, n = 4).

4.4. Zircon Hf—O isotopes

New zircon Hf—O isotope compositions for the Maoding intrusion are presented in Table 3 and Fig. 8. They show homogenous $\varepsilon_{Hf}(t)$ values of 14.3 ± 0.6 (weighted mean values, 2σ; n = 19), with young two-stage Hf model ages of 287 ± 82 Ma (n = 19). Maoding has relatively low zircon $\delta^{18}O$ ratios from 5.6‰ to 7.9‰ (avg. = 6.3 ± 0.6‰, n = 15; Table 3).

4.5. Zircon and apatite compositions

The compositions of zircon and apatite from the Baimaxueshan, Suwalong, and Maoding granitoids are listed in digital Appendix Tables A4 and A5, respectively.

4.5.1. Zircon trace element compositions

Twenty-five trace element spot analyses were obtained on zircon for each sample from the Baimaxueshan (BMXS17–1 and BMXS17–7) and Suwalong (SWL17–2, SWL17–3, SWL17–5) intrusions. For the Maoding intrusion (MD12–2), fifteen zircon grains were analyzed (digital App. Table A4).

The remaining analyses for the three granitic intrusions have high HREE and low LREE concentrations, with negative Eu and positive Ce anomalies (Fig. 9). These REE patterns (ΣREE = 158–2515 ppm) with Th/U ratios above 0.1 (0.15–0.56) are consistent with igneous zircons

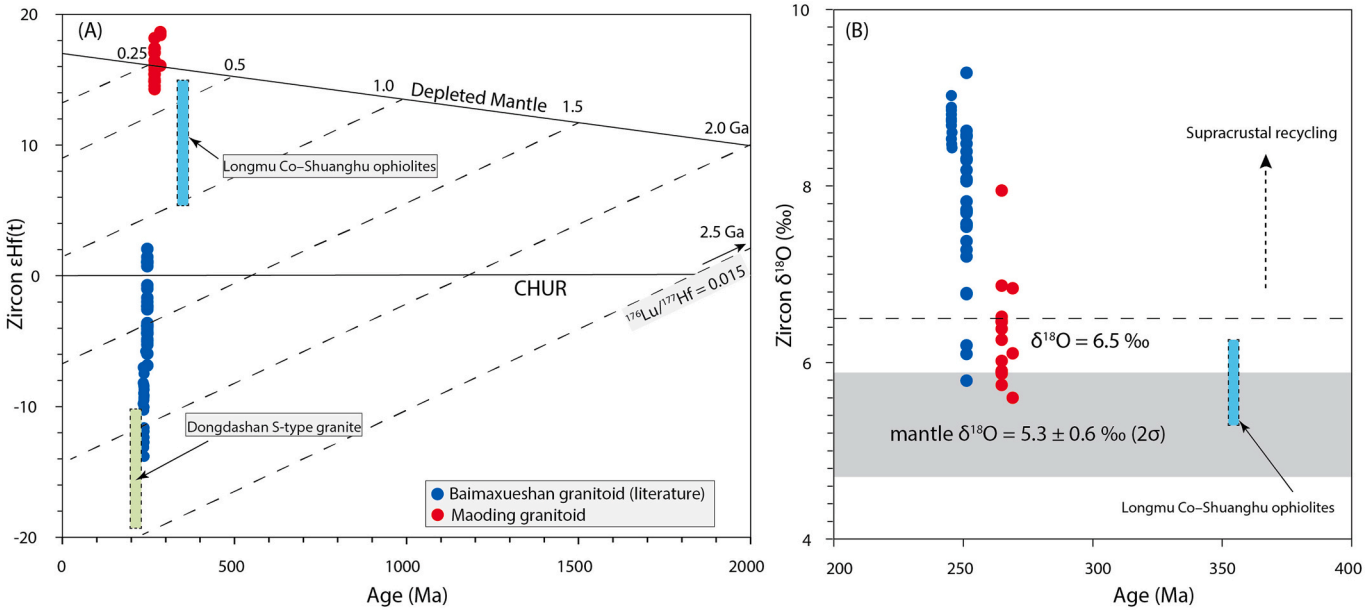

Fig. 8. (A) $\varepsilon_{Hf}(t)$ and (B) $\delta^{18}O$ values vs. U—Pb ages of zircon grains from the Baimaxueshan, Suwalong, and Maoding granitoids. Data sources for the Baimaxueshan intrusion from Zi et al. (2012a) and He et al. (2018). The light gray band in B represents the range of igneous zircons in high-temperature equilibrium with the mantle ($\delta^{18}O = 5.3 \pm 0.6‰$, 2σ; Valley et al., 1998). Zircon $\delta^{18}O$ values above 6.5‰ indicate significant contamination of supracrustal material.

(Hoskin and Schaltegger, 2003).

Titanium-in-zircon temperatures were calculated using the method of Ferry and Watson (2007); T_{Zr}; Fig. 10A)). Because of the existence of quartz and titanite in the host intrusions, it is assumed that log $a_{SiO2} = 1$ and log $a_{TiO2} = 0.7$. The Baimaxueshan zircon grains have the lowest T_{Zr} values of 704 ± 29 °C (range = 644°–766 °C, n = 17), with Eu_N/Eu_N^* of 0.36 ± 0.12 (range = 0.20–0.56, n = 17). Zircon grains from the Suwalong intrusion have T_{Zr} values of 788 ± 30 °C (range = 682°–851 °C, *n* = 54) and Eu_N/Eu_N^* ratios of 0.26 ± 0.07 (range = 0.15–0.47, n = 54). Zircon grains from the Maoding intrusion yielded calculated temperatures of 725 ± 38 °C (T_{Zr} = 660°–781 °C, *n* = 22) and Eu_N/Eu_N^* values of 0.28 ± 0.12 (range = 0.15–0.47, n = 15).

4.5.2. *Apatite compositions*

The SO_3 analyses of igneous apatite are provided in digital Appendix Table A5 and Fig. 11. All the analyzed apatite microphenocrysts are enclosed within primary minerals including amphibole, plagioclase, and biotite (Fig. 11). None of them contain patchy zoning and porous textures, indicative of an igneous origin (Bouzari et al., 2016). Apatite crystals from the Maoding, Suwalong, and Baimaxueshan intrusions have extremely low sulfur contents, most of which are lower than the analytical detection limit (D.L. = 0.12 wt% SO_3 for the Baimaxueshan and Suwalong intrusions, and 0.04 wt% SO_3 for the Maoding intrusion; Fig. 11; digital App. Table A5).

5. Discussion

5.1. *Timing and petrogenesis*

Three granitic intrusions from the Jiangda–Weixi Arc belt have yielded ages of 268.3 ± 2.3 Ma, 275.6 ± 1.4 Ma to 264.7 ± 1.4 Ma, and 255.7 ± 1.5 Ma to 249.3 ± 1.1 Ma for the Maoding, Suwalong, and Baimaxueshan granitoids, respectively (Fig. 4). The Suwalong and Baimaxueshan intrusions were emplaced over a time span of ~11 and 6 Myr, respectively, which are consistent with the ~7 to 15 Myr zircon crystallization periods for many porphyry plutons worldwide (Loucks, 2021). Loucks (2021) has further explained such multi-million-year zircon U—Pb age spans within individual plutons by their derivation from long-term and deep-seated differentiation of magmas, probably also applicable to the Suwalong and Baimaxueshan granitoids. Published age data show that the Tongpu granitoid (Fig. 1) and Jiyidu tonalite (Fig. 2) in the Jiangda–Weixi Arc belt formed at ~263 Ma and ~ 283 Ma (zircon U—Pb dating; Zi et al., 2012b; Wu et al., 2013). In combination with the widespread Early Permian to Early Triassic volcanic rocks and ultramafic–mafic intrusions, a long-lived arc (~40–50 Ma) has been identified, likely related to subduction of the Paleo-Tethyan Ocean (Figs. 1 and 16B; Yang et al., 2014; Xin et al., 2018; Wang et al., 2020; Metcalfe, 2021).

The Maoding, Suwalong, and Baimaxueshan intrusions show similar whole-rock major and trace element compositions, with typical features of subduction derived rocks characterized by high LILE and low HFSE abundances (Figs. 5–6; Pearce, 1996). They are mostly felsic, metaluminous to slightly peraluminous, and calc-alkaline in composition. The geochemistry of the rocks is consistent with partial melting of the mantle wedge, mixed with variable degrees of lower crust-derived melts likely as a result of MASH processes (melting, assimilation, storage, and homogenization) as has been suggested for the generation of continental arc magmas (Audétát and Simon, 2012; Richards, 2003).

The Maoding and Suwalong intrusions have mantle-like Sr—Nd isotopic compositions, typified by relatively low initial Sr isotope ratios and high $\varepsilon_{Nd}(t)$ values [$(^{87}Sr/^{86}Sr)_t$ = 0.7043–0.7057; $\varepsilon_{Nd}(t)$ = +0.4 to +2.8; Fig. 7]. Zircon crystals from the Maoding intrusion show positive $\varepsilon_{Hf}(t)$ values (14.3 ± 0.6) and mantle-like $\delta^{18}O$ ratios (6.3 ± 0.6 ‰; Fig. 8; Valley et al., 1998), with juvenile single-stage Hf model ages (287 ± 82 Ma). This suggests limited involvement of ancient crustal components in the generation of the Maoding and Suwalong granitoids and is consistent with the positive $\varepsilon_{Nd}(t)$ values. In contrast, the younger Baimaxueshan granitoid shows relatively high $(^{87}Sr/^{86}Sr)_t$ (0.7097–0.7128) and negative $\varepsilon_{Nd}(t)$ (−10.7 to −6.7) values (Fig. 7), consistent with contamination by older crust. Crustal contamination is supported by the presence of numerous xenocrystic and/or inherited zircon grains (digital App. Table A2). Modelling of Sr—Nd isotopic mixing suggests ~30% crustal contamination for the Baimaxueshan but minor (<5%) for the Maoding and Suwalong intrusions with the most likely contaminant being Eastern Qiangtang crust (Peng et al., 2015; Fig. 7). This is also supported by published zircon Hf—O isotope compositions for the Baimaxueshan granitoid which show negative zircon $\varepsilon_{Hf}(t)$ ratios (mostly < −5), higher $\delta^{18}O$ values (mostly >7‰), and older

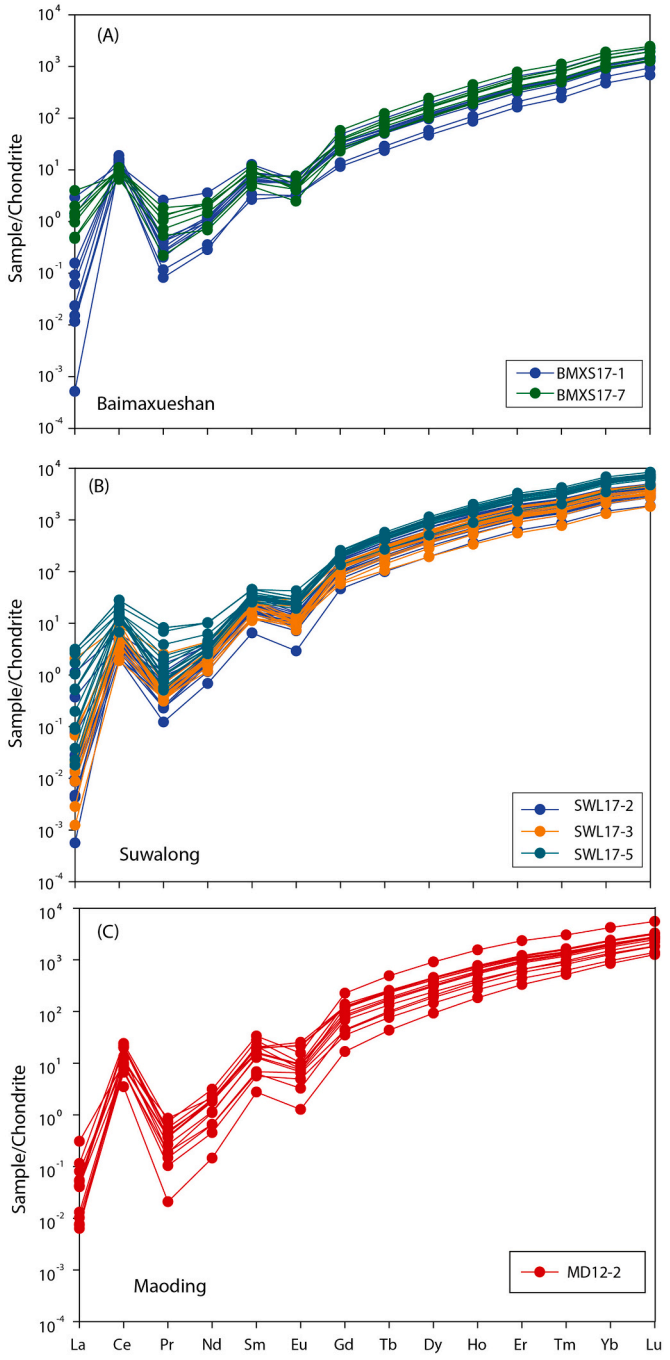

Fig. 9. Chondrite-normalized REE patterns for zircons from (A) the Baimaxueshan, (B) Suwalong, and (C) Maoding granitoids. Normalizing values from Sun and McDonough (1989).

single-stage Hf model ages (> 1 Ga; Fig. 8A; Zi et al., 2012a; He et al., 2018). The increase in crustal assimilation in the Jiangda–Weixi Arc granitoids over time has been observed in other continental arc settings (e.g., Myanmar, Licht et al., 2020; central Andes, Capaldi et al., 2021), probably due to the thickening of the overlying terrane. This is consistent with that elevated La/Yb for the Baimaxueshan granitoid (avg. = 23.3 ± 6.5) than the Maoding (avg. = 12.7 ± 6.6) and Suwalong (avg. = 16.3 ± 6.8) intrusions, as La/Yb in magmatic arcs are commonly correlated to crustal thickness globally (Profeta et al., 2015). Given the crust-derived melts in the Eastern Qiangtang show relatively low Sr/Y ratios (<10; Peng et al., 2015), the increasing crustal assimilation may be also accountable for the lower Sr/Y values of the Baimaxueshan granitoid (avg. = 19.2 ± 5.3) than the Maoding (avg. = 64.3 ± 16.2) and Suwalong (avg. = 32.7 ± 9.5) intrusions. In summary, the three granitoids were all derived from the mixing of mantle and variable degree of crustal magmas, consistent with typical continental arc igneous rocks worldwide.

5.2. Magma fertility

Magmatic water contents: It is difficult to accurately estimate original magmatic water contents, although a few methods have been proposed that use mineral geochemistry (e.g., amphibole and plagioclase; Ridolfi et al., 2010; Waters and Lange, 2015). Li and Costa (2020) have provided a thermodynamic model for F-Cl-OH partitioning between apatite and silicate melts, which can be applied to constrain melt water contents. However, the known concentrations of Cl and/or F in the melt are necessary, which are not available here. A number of lines of evidence suggest that the causative magmas related to the Baimaxueshan, Suwalong and Maoding intrusions were water-rich. Amphibole or biotite crystals are abundant in these intrusions, and some amphibole or biotite crystals occur as inclusions within plagioclase grains. This suggests the amphibole or biotite crystallized earlier than plagioclase, consistent with hydrous melts (> 4 wt%;). Their high whole-rock Sr/Y ratios (35 ± 20, $n = 17$; Fig. 5B), roughly negative correlation between SiO_2 and Dy/Yb ratios, lack of negative Eu anomalies ($Eu_N/Eu_N^* = 1.04 \pm 0.3$; Fig. 5D), flat- to listric-shaped REE patterns (Fig. 6B), and zircon Dy/Yb < 0.3 (0.24 ± 0.06, $n = 101$) are all consistent with hydrous magmas that underwent no early plagioclase crystallization but abundant amphibole fractionation (Loucks, 2014; Lu et al., 2016; Moore and Carmichael, 1998). Eventually, the high magmatic water contents might be coupled with chemical differentiation of melts at high pressure (i.e., high dissolved water at high pressure; e.g., Loucks, 2021).

Magmatic oxygen fugacity: It is equally difficult to measure the original magmatic oxygen fugacity (Zou et al., 2019). The Baimaixueshan, Suwalong, and Maoding intrusions are ilmenite-series granite (Fig. 3E–F), broadly indicative of derivation from reduced magmas. Zircon compositions have been widely used to provide qualitative estimates of magmatic oxygen fugacity and to potentially identify fertile suites in porphyry Cu systems (Ballard et al., 2002; Dilles et al., 2015; Loucks et al., 2020; Zhu et al., 2018). Europium is preferably partitioned into zircon as Eu^{3+} in oxidized magmas (Ballard et al., 2002; Hoskin and Schaltegger, 2003), whereas in hydrous magmas, the suppression of early plagioclase crystallization would lead to high Eu_N/Eu_N^* values (Moore and Carmichael, 1998). As a result relatively high zircon Eu_N/Eu_N^* ratios (>0.4) have been interpreted as an indicator of relatively high magmatic oxidation states and/or water contents (Dilles et al., 2015; Lu et al., 2016). Zircons from the Baimaxueshan, Suwalong, and Maoding intrusions have relatively low Eu_N/Eu_N^* ratios (mostly <0.4), consistent with relatively low oxygen fugacity and/or low water contents in the melts. As the mineral chemistry of the arc granitoids in the Jiangda–Weixi belt suggests that they were derived from hydrous melts, the variation of zircon Eu_N/Eu_N^* values might partly reflect differences in the oxidation state of the magmas.

The zircon Ce^{4+}/Ce^{3+} ratio defined by Ballard et al. (2002) has been widely used as a proxy for magmatic oxygen fugacity. However, it is difficult to estimate Ce^{4+}/Ce^{3+} due to a number of issues and this often yields anomalous ΔFMQ values (ΔFMQ −8 to +10; Dilles et al., 2015; Lu et al., 2016; Zhu et al., 2018; Zou et al., 2019). Lanthium and Pr are used to calculate the Ce anomaly but their abundance in zircons is often too low to be measured accurately. In the present study, Ce^{4+}/Ce^{3+} ratios and calculated fO_2 values determined using the methods of Trail et al. (2012) yielded unrealistic ΔFMQ values of −5 to +8. Loucks et al. (2020) proposed a novel method for determining magmatic fO_2 (± 0.6 logarithmic unit fO_2) using Ce, U, and Ti in zircon. This method can give valid results and has been successfully used to identify fertile porphyry systems (e.g., Meng et al., 2021; Wang et al., 2021). Using this new-derived method, the Baimaxueshan, Suwalong, and Maoding

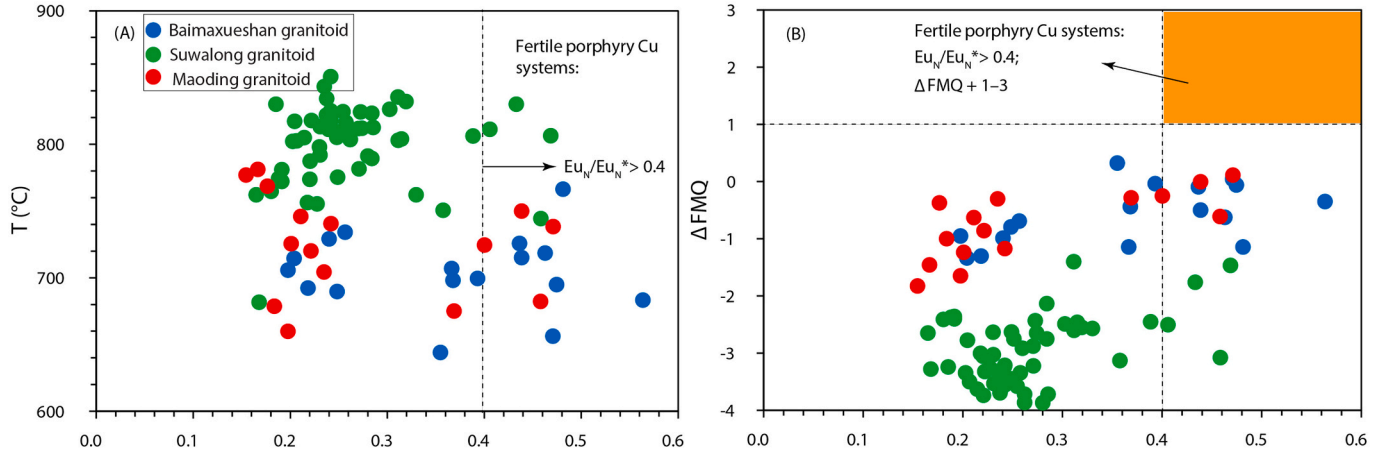

Fig. 10. Plots of zircon Eu_N/Eu_N^* vs. (A) temperatures and (B) ΔFMQ values. $Eu_N/Eu_N^*$is the europium anomaly, calculated as $Eu_N/Eu_N^* = Eu_N/(Sm_N \times Gd_N)^{0.5}$, using the chondrite normalization values of Sun and McDonough (1989). Temperatures calculated using Ti-in-zircon thermometer by Ferry and Watson (2007): log (ppm Ti-in-zircon) = (5.711 ± 0.072) –(4800 ± 86)/T (K) - log a_{SiO2} + log a_{TiO2}, wherein log a_{SiO2} = 1 because of the existence of quartz, and log a_{TiO2} = 0.7 due to the present of the titanite. ΔFMQ values calculated following the method of Loucks et al. (2020). Field for fertile porphyry Cu systems compiled from literature (Dilles et al., 2015; Richards, 2015a; Richards et al., 2017; Tang et al., 2020; Wang et al., 2018b; Zhu et al., 2018). See text for details.

granitoids yielded ΔFMQ values of −0.6 ± 0.5 (n = 17), −3.0 ± 0.6 (*n* = 54), and − 0.8 ± 0.6 (*n* = 15), respectively, indicative of derivation from reduced magmas (digital Appendix Table A4).

The sulfur content in apatite is controlled by oxygen fugacity, temperature, and the S content in the associated melt (Konecke et al., 2019; Parat et al., 2011; Webster and Piccoli, 2015). The incorporation of sulfur into the apatite structure mainly replaces P and/or Ca as sulfate ions (S^{6+}) in relatively oxidized conditions (Parat et al., 2011; Piccoli and Candela, 2002), although recent studies have shown that apatite crystallized from reduced magmas could contain minor amounts of S, where S occurred as sulfide ions (S^{2-}; Konecke et al., 2019). It is widely accepted that the sulfur species in silicic melts changes from S^{2-} to S^{6+} with increasing magmatic oxygen fugacity (Jugo et al., 2010; Konecke et al., 2019; Tang et al., 2020). Consequently, apatite formed in reduced conditions would have low sulfur contents regardless of the amount of sulfur dissolved in the melt. As most of apatite SO_3 contents in rocks from this study are lower than the analytical detection limit, it is impossible to calculate accurate magmatic fO_2 using apatite S^{6+}/S^{2-} ratios (Konecke et al., 2019; Meng et al., 2021). But the very low sulfur contents in apatite from the three arc granitoids suggest a low magmatic oxygen fugacity (Fig. 11; digital App. Table A5). Taken together, the geochemical compositions of zircon and apatite, suggest that the magmas associated with arc suites in the Jiangda–Weixi belt were reduced.

5.3. Metallogenic implications

The Permian to Early Triassic igneous rocks related to subduction of the Paleo-Tethyan Ocean are widespread in the Jiangda–Weixi Arc belt but host only rare porphyry Cu deposits (Figs. 1 and 2). The scarcity of porphyry deposits in the belt might be explained by uplift of the Tibetan plateau and subsequent exhumation, however, voluminous coeval volcanic rocks in the Jiangda–Weixi belt suggest that erosion alone cannot fully account for the scarcity of porphyry Cu deposits associated in the Sanjiang region (Fig. 1). The generative magmas of the granitic rocks were generally enriched in water (> 4 wt%), consistent with typical arc and fertile porphyry magmas (Plank et al., 2013; Rezeau and Jagoutz, 2020; Richards, 2015a). However, compared with fertile porphyry systems worldwide (fO_2 = ΔFMQ +1 to +3 with zircon $Eu_N/Eu_N^* > 0.4$ and apatite SO_3 > 0.2 wt%; Dilles et al., 2015; Richards, 2015a; Richards et al., 2017; Wang et al., 2018b; Zhu et al., 2018; Tang et al., 2020), they are relatively reduced (ΔFMQ = −2.1 ± 1.2, n = 101; Fig. 10), which would result in extensive separation of sulfide phases in the melts and loss of chalcophile metals such as Cu (Jugo et al., 2010; Sun et al., 2015). This would limit the fertility for porphyry Cu formation in the Paleo-Tethyan arc belt. Therefore, the magmatic fO_2 rather than water content might play as a critical control on the prospectivity of arc systems.

The Paleo-Tethyan arc in SE Asia is the most productive region for Sn around the world (e.g., Malaysia, Thailand; Romer and Kroner, 2016; Yang et al., 2020). As Sn^{2+} is incompatible in reduced magma and sequestered as Sn^{4+} by Sn-bearing minerals (Lehmann, 2021), reduced magmas can transport Sn and their presence favours the formation of Sn deposits. The presence of Sn deposits therefore is consistent with reduced magmas in the Paleo-Tethyan arc. It is important noting that reduced magmas solely cannot make a magmatic-hydrothermal Sn deposit. Other parameters such as degree of fractionation and nature of the protolith are also of importance for Sn deposit formation (Lehmann, 2021; Zhao et al., 2022).

6. Conclusions

The geochemical compositions and magmatic fertilities of the Permian–Early Triassic igneous rocks in the Sanjiang region, show that the ~275–249 Ma granitoids in the Jiangda–Weixi Arc belt were derived from partial melting of the mantle wedge, that mixed with increased amounts of crust-derived melts over time. Our work shows that the eastern Paleo-Tethyan arc magmas were hydrous but relatively reduced and therefore less fertile for porphyry Cu deposits formation.

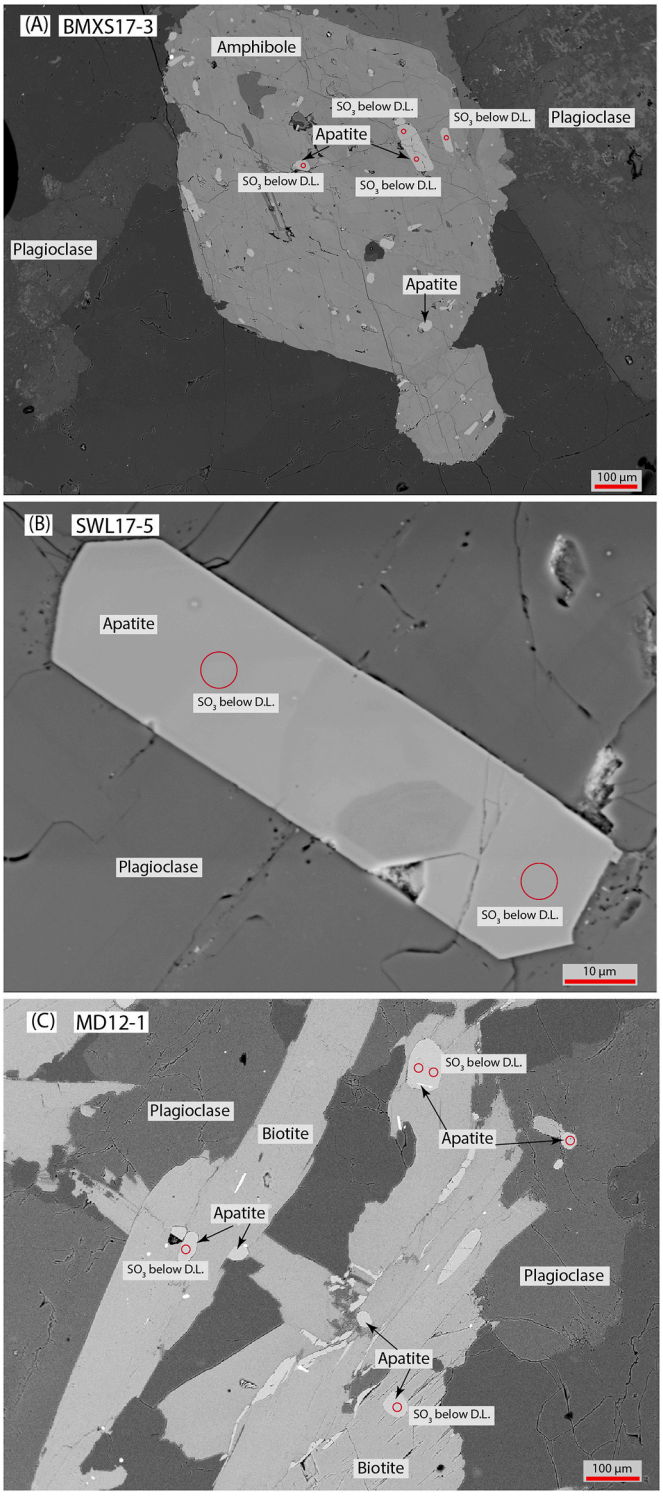

Fig. 11. Backscattered electron images of apatite crystals in samples from (A) Baimaxueshan (BMXS17–3), (B) Suwalong (SWL17–5), and (C) Maoding (MD12–1) granitoids. Red circles show the analyzed spots. Concentrations of apatite SO_3 most below the detection limit (D.L. = 0.12 wt% SO_3 for the Baimaxueshan and Suwalong intrusions, and 0.04 wt% SO_3 for the Maoding intrusion). (For interpretation of the references to colour in this figure legend, the reader is referred to the web version of this article.)

Declaration of Competing Interest

The authors declare that they have no known competing financial interests or personal relationships that could have appeared to influence the work reported in this paper.

Acknowledgements

This work was jointly funded by the project of "Innovative Team of One Belt and One Road" of the Chinese Academy of Sciences, the National Natural Science Foundation of China (42073047, 91955209, 41673049, 42121003), and the K.C. Wong Education Foundation (GJTD-2020-13) and Hundred Talent Plan of the Chinese Academy of Sciences. Prof. Di-Cheng Zhu is thanked for editorial suggestion and efficient handling of this manuscript. We also thank Profs. R. R. Loucks and Xiang Sun for constructive reviews.

Appendix A. Supplementary data

Supplementary data to this article can be found online at https://doi.org/10.1016/j.lithos.2022.106775.

References

Audétát, A., Simon, A.C., 2012. Magmatic controls on porphyry copper genesis. Soc. Econ. Geol. Spec. Publ. 16, 553–572.
Ballard, J.R., Palin, M.J., Campbell, I.H., 2002. Relative oxidation states of magmas inferred from $Ce^{(IV)}/Ce^{(III)}$ in zircon: application to porphyry copper deposits of northern Chile. Contrib. Mineral. Petrol. 144, 347–364.
Bouzari, F., Hart, C.J., Bissig, T., Barker, S., 2016. Hydrothermal alteration revealed by apatite luminescence and chemistry: a potential indicator mineral for exploring covered porphyry copper deposits. Econ. Geol. 111, 1397–1410.
Cao, K., Yang, Z.-M., Mavrogenes, J., White, N., Xu, J.F., Li, Y., Li, W.K., 2019. Geology and genesis of the giant Pulang porphyry Cu-Au district, Yunnan, Southwest China. Econ. Geol. 114, 275–301.
Capaldi, T.N., McKenzie, N.R., Horton, B.K., Mackaman-Lofland, C., Colleps, C.L., Stockli, D.F., 2021. Detrital zircon record of Phanerozoic magmatism in the southern Central Andes. Geosphere 17, 876–897.
Cooke, D.R., Hollings, P., Walshe, J.L., 2005. Giant porphyry deposits: characteristics, distribution, and tectonic controls. Econ. Geol. 100, 801–818.
Deng, J., Wang, Q., Li, G., Li, C., Wang, C., 2014. Tethys tectonic evolution and its bearing on the distribution of important mineral deposits in the Sanjiang region, SW China. Gondwana Res. 26, 419–437.
Dilles, J.H., Kent, A.J., Wooden, J.L., Tosdal, R.M., Koleszar, A., Lee, R.G., Farmer, L.P., 2015. Zircon compositional evidence for sulfur-degassing from ore-forming arc magmas. Econ. Geol. 110, 241–251.
Evans, K.A., Tomkins, A.G., 2011. The relationship between subduction zone redox budget and arc magma fertility. Earth Planet. Sci. Lett. 308, 401–409.
Ferry, J., Watson, E., 2007. New thermodynamic models and revised calibrations for the Ti-in-zircon and Zr-in-rutile thermometers. Contrib. Mineral. Petrol. 154, 429–437.
He, W.-Y., Yang, L.Q., Lu, Y.J., Jeon, H., Xie, S., Gao, X., 2018. Zircon U-Pb dating, geochemistry and Sr–Nd–Hf–O isotopes for the Baimaxueshan granodiorites and mafic microgranulars enclaves in the Sanjiang Orogen: evidence for westward subduction of Paleo-Tethys. Gondwana Res. 62, 112–126.
Hoskin, P.W., Schaltegger, U., 2003. The composition of zircon and igneous and metamorphic petrogenesis. Rev. Mineral. Geochem. 53, 27–62.
Hou, Z.Q., Yang, Z.M., Lu, Y.J., Kemp, A., Zheng, Y., Li, Q., Tang, J., Yang, Z., Duan, L., 2015. A genetic linkage between subduction-and collision-related porphyry Cu deposits in continental collision zones. Geology 43, 247–250.
Jian, P., Liu, D., Sun, X., 2003. SHRIMP dating of Baimaxueshan and Ludian granitoid batholiths, northwestern Yunnan province, and its geological implications. Acta Geosci. Sin. 24, 337–342 (in Chinese with English abstract).
Jugo, P.J., Wilke, M., Botcharnikov, R.E., 2010. Sulfur K-edge XANES analysis of natural and synthetic basaltic glasses: implications for S speciation and S content as function of oxygen fugacity. Geochim. Cosmochim. Acta 74, 5926–5938.
Kelley, K.A., Cottrell, E., 2009. Water and the oxidation state of subduction zone magmas. Science 325, 605–607.
Keto, L.S., Jacobsen, S.B., 1987. Nd and Sr isotopic variations of Early Paleozoic oceans. Earth Planet. Sci. Lett. 84, 27–41.
Konecke, B.A., Fiege, A., Simon, A.C., Linsler, S., Holtz, F., 2019. An experimental calibration of a sulfur-in-apatite oxybarometer for mafic systems. Geochim. Cosmochim. Acta 265, 242–258.
Lehmann, B., 2021. Formation of tin ore deposits: a reassessment. Lithos 402–403, 105756.
Li, W.R., Costa, F., 2020. A thermodynamic model for F-Cl-OH partitioning between silicate melts and apatite including non-ideal mixing with application to constraining melt volatile budgets. Geochim. Cosmochim. Acta 269, 203–222.
Li, C., Zhai, Q., Dong, Y., Huang, X., 2006. Discovery of eclogite and its geological significance in Qiangtang area, Central Tibet. Chin. Sci. Bull. 51, 1095–1100.

Licht, A., Win, Z., Westerweel, J., Cogné, N., Morley, C.K., Chantraprasert, S., Poblete, F., Ugrai, T., Nelson, B., Aung, D.W., Dupont-Nivet, G., 2020. Magmatic history of Central Myanmar and implications for the evolution of the Burma Terrane. Gondwana Res. 87, 303–319.
Loucks, R.R., 2014. Distinctive composition of copper-ore-forming arcmagmas. Aust. J. Earth Sci. 61, 5–16.
Loucks, R.R., 2021. Deep entrapment of buoyant magmas by orogenic tectonic stress: its role in producing continental crust, adakites, and porphyry copper deposits. Earth Sci. Rev. 220, 103744.
Loucks, R.R., Fiorentini, M.L., Henríquez, G.J., 2020. New magmatic oxybarometer using trace elements in zircon. J. Petrol. 61 egaa034.
Lu, Y.-J., Loucks, R.R., Fiorentini, M., McCuaig, T.C., Evans, N.J., Yang, Z.-M., Hou, Z.-Q., Kirkland, C.L., Parra-Avila, L.A., Kobussen, A., 2016. Zircon compositions as a pathfinder for porphyry Cu±Mo±Au deposits. Soc. Econ. Geol. Spec. Publ. 19, 329–347.
Meng, X., Kleinsasser, J.M., Richards, J.P., Tapster, S.R., Jugo, P.J., Simon, A.C., Kontak, D.J., Robb, L., Bybee, G.M., Marsh, J.H., Stern, R.A., 2021. Oxidized sulfur-rich arc magmas formed porphyry Cu deposits by 1.88 Ga. Nat. Commun. 12, 2189.
Metcalfe, I., 2021. Multiple Tethyan Ocean basins and orogenic belts in Asia. Gondwana Res. 100, 87–130.
Middlemost, E.A.K., 1994. Naming materials in the magma/igneous rock system. Earth-Sci. Rev. 37, 215–224.
Mo, X.X., Lu, F.X., Shen, S.Y., Zhu, Q.W., Hou, Z.Q., Yang, K.H., Deng, J.F., Liu, X.P., He, C.X., Lin, P.Y., Zhang, B.M., Tai, D.Q., Chen, M.H., Hu, X.S., Ye, S., Xue, Y.X., Tan, J., Wei, Q.R., Fan, L., 1993. Sanjiang Tethyan Volcanism and Related Mineralization. Geological Publishing House, Beijing, 276 pp. (in Chinese).
Moore, G., Carmichael, I., 1998. The hydrous phase equilibria (to 3 kbar) of an andesite and basaltic andesite from western Mexico: constraints on water content and conditions of phenocryst growth. Contrib. Mineral. Petrol. 130, 304–319.
Parat, F., Holtz, F., Klügel, A., 2011. S-rich apatite-hosted glass inclusions in xenoliths from La Palma: constraints on the volatile partitioning in evolved alkaline magmas. Contrib. Mineral. Petrol. 162, 463–478.
Pearce, J., 1996. Sources and settings of granitic rocks. Episodes 19, 120–125.
Peng, T., Zhao, G., Fan, W., Peng, B., Mao, Y., 2015. Late Triassic granitic magmatism in the Eastern Qiangtang, Eastern Tibetan Plateau: geochronology, petrogenesis and implications for the tectonic evolution of the Paleo-Tethys. Gondwana Res. 27, 1494–1508.
Piccoli, P.M., Candela, P.A., 2002. Apatite in igneous systems. Rev. Mineral. Geochem. 48, 255–292.
Plank, T., Langmuir, C.H., 1998. The chemical composition of subducting sediment and its consequences for the crust and mantle. Chem. Geol. 145, 325–394.
Plank, T., Kelley, K.A., Zimmer, M.M., Hauri, E.H., Wallace, P.J., 2013. Why do mafic arc magmas contain ~4wt% water on average? Earth Planet. Sci. Lett. 364, 168–179.
Profeta, L., Ducea, M.N., Chapman, J.B., Paterson, S.R., Gonzales, S.M., Kirsch, M., Petrescu, L., DeCelles, P.G., 2015. Quantifying crustal thickness over time in magmatic arcs. Sci. Report. 5, 17786.
Rezeau, H., Jagoutz, O., 2020. The importance of H_2O in arc magmas for the formation of porphyry Cu deposits. Ore Geol. Rev. 126, 103744.
Richards, J.P., 2003. Tectono-magmatic precursors for porphyry Cu-(Mo-Au) deposit formation. Econ. Geol. 98, 1515–1533.
Richards, J.P., 2013. Giant ore deposits formed by optimal alignments and combinations of geological processes. Nat. Geosci. 6, 911–916.
Richards, J.P., 2015a. The oxidation state, and sulfur and Cu contents of arc magmas: implications for metallogeny. Lithos 233, 27–45.
Richards, J.P., 2015b. Tectonic, magmatic, and metallogenic evolution of the Tethyan orogen: from subduction to collision. Ore Geol. Rev. 70, 323–345.
Richards, J.P., Şengör, A.C., 2017. Did Paleo-Tethyan anoxia kill arc magma fertility for porphyry copper formation? Geology 45, 591–594.
Richards, J.P., López, G.P., Zhu, J.-J., Creaser, R.A., Locock, A.J., Mumin, A.H., 2017. Contrasting tectonic settings and sulfur contents of magmas associated with cretaceous porphyry Cu ± Mo ± Au and intrusion-related iron oxide Cu-Au deposits in Northern Chile. Econ. Geol. 112, 295–318.
Ridolfi, F., Renzulli, A., Puerini, M., 2010. Stability and chemical equilibrium of amphibole in calc-alkaline magmas: an overview, new thermobarometric formulations and application to subduction-related volcanoes. Contrib. Mineral. Petrol. 160, 45–66.
Romer, R.L., Kroner, U., 2016. Phanerozoic tin and tungsten mineralization—Tectonic controls on the distribution of enriched protoliths and heat sources for crustal melting. Gondwana Res. 31, 60–95.
SCBGMR (Bureau of Geology and Mineral Resources of Sichuan Province), 1977. Geological Map of the Sichuan Province, Sheet H-47-XXII (Bomi) Scale 1: 200,000.
Sillitoe, R.H., 2010. Porphyry copper systems. Econ. Geol. 105, 3–41.
Sillitoe, R.H., 2018. Why no porphyry copper deposits in Japan and South Korea? Resour. Geol. 68, 107–125.
Sun, S.-S., McDonough, W., 1989. Chemical and isotopic systematics of oceanic basalts: implications for mantle composition and processes. Geol. Soc. Lond. Spec. Publ. 42, 313–345.
Sun, W., Huang, R.-F., Li, H., Hu, Y.-B., Zhang, C.-C., Sun, S.-J., Zhang, L.-P., Ding, X., Li, C.-Y., Zartman, R.E., Ling, M.-X., 2015. Porphyry deposits and oxidized magmas. Ore Geol. Rev. 65, 97–131.
Tang, M., Lee, C.-T.A., Ji, W.-Q., Wang, R., Costin, G., 2020. Crustal thickening and endogenic oxidation of magmatic sulfur. Sci. Adv. 6, eaba6342.
Tera, F., Wasserburg, G., 1972. U-Th-Pb systematics in three Apollo 14 basalts and the problem of initial Pb in lunar rocks. Earth Planet. Sci. Lett. 14, 2311–2323.
Trail, D., Bruce Watson, E., Tailby, N.D., 2012. Ce and Eu anomalies in zircon as proxies for the oxidation state of magmas. Geochim. Cosmochim. Acta 97, 70–87.
Valley, J.W., Kinny, P.D., Schulze, D.J., Spicuzza, M.J., 1998. Zircon megacrysts from kimberlite: oxygen isotope variability among mantle melts. Contrib. Mineral. Petrol. 133, 1–11.
Wang, Y.-J., Qian, X., Cawood, P.A., Liu, H., Feng, Q., Zhao, G., Zhang, Y., He, H., Zhang, P., 2018a. Closure of the East Paleotethyan Ocean and amalgamation of the Eastern Cimmerian and Southeast Asia continental fragments. Earth Sci. Rev. 186, 195–230.
Wang, R., Weinberg, R.F., Collins, W.J., Richards, J.P., Zhu, D.-C., 2018b. Origin of postcollisional magmas and formation of porphyry Cu deposits in southern Tibet. Earth Sci. Rev. 181, 122–143.
Wang, Y.N., Xue, S.C., Deng, J., Wang, Q.F., Li, C., Ripley, E.M., 2020. Triassic arc mafic magmatism in North Qiangtang: implications for tectonic reconstruction and mineral exploration. Gondwana Res. 82, 337–353.
Wang, D.-Z., Hu, R., Hollings, P., Bi, X.-W., Zhong, H., Pan, L.-C., Leng, C.-B., Huang, M.-L., Zhu, J.-J., 2021. Remelting of a Neoproterozoic arc root: origin of the Pulang and Songnuo porphyry Cu deposits, Southwest China. Mineral. Deposita 56, 1043–1070.
Waters, L.E., Lange, R.A., 2015. An updated calibration of the plagioclase-liquid hygrometer-thermometer applicable to basalts through rhyolites. Am. Mineral. 100, 2172–2184.
Webster, J.D., Piccoli, P.M., 2015. Magmatic apatite: a powerful, yet deceptive, mineral. Elements v. 11, 177–182.
Wu, T., Xiao, L., Ma, C., Huang, W., 2013. The geochronological, geochemical, and Sr-Nd isotopic characteristics of Tongpu intrusive complex and its implications. Acta Petrol. Sin. 29, 3567–2580 (in Chinese with English abstract).
Xin, D., Yang, T.N., Liang, M.J., Xue, C.D., Han, X., Liao, C., Tang, J., 2018. Syn-subduction crustal shortening produced a magmatic flare-up in middle Sanjiang orogenic belt, southeastern Tibet Plateau: evidence from geochronology, geochemistry, and structural geology. Gondwana Res. 62, 93–111.
Xu, Z., Dilek, Y., Cao, H., Yang, J., Robinson, P., Ma, C., Li, H., Jolivet, M., Roger, F., Chen, X., 2015. Paleo-Tethyan evolution of Tibet as recorded in the East Cimmerides and West Cathaysides. J. Asian Earth Sci. 105, 320–337.
Yang, Z.M., Cooke, D.R., 2019. Porphyry copper deposits in China. Soc. Econ. Geol. Spec. Publ. 22, 133–187.
Yang, T.N., Zhang, H.R., Liu, Y., Wang, Z., Song, Y., Yang, Z., Tian, S., Xie, H., Hou, K., 2011. Permo-Triassic arc magmatism in central Tibet: evidence from zircon U–Pb geochronology, Hf isotopes, rare earth elements, and bulk geochemistry. Chem. Geol. 284, 270–282.
Yang, T.N., Ding, Y., Zhang, H.R., Fan, J., Liang, M., Wang, X., 2014. Two-phase subduction and subsequent collision defines the Paleotethyan tectonics of the southeastern Tibetan Plateau: evidence from zircon U-Pb dating, geochemistry, and structural geology of the Sanjiang orogenic belt, Southwest China. Geol. Soc. Am. Bull. 126, 1654–1682.
Yang, J.-H., Zhou, M.-F., Hu, R.-Z., Zhong, H., Williams-Jones, A.E., Liu, L., Zhang, X.-C., Fu, Y.-Z., Mao, W., 2020. Granite-related tin metallogenic events and key controlling factors in Peninsular Malaysia, Southeast Asia: new insights from cassiterite U-Pb dating and zircon geochemistry. Econ. Geol. 115, 581–601.
Zhai, Q.-G., Chung, S.-L., Tang, Y., Hu, P.-Y., Jin, X.-C., Wang, J., Wang, H.-T., Wang, K.-L., Lee, H.-Y., 2019. Late Carboniferous ophiolites from the southern Lancangjiang belt, SW China: implication for the arc–back-arc system in the eastern Paleo-Tethys. Lithos 344–345, 134–146.
Zhang, K.-J., Tang, X.-C., Wang, Y., Zhang, Y.-X., 2011. Geochronology, geochemistry, and Nd isotopes of early Mesozoic bimodal volcanism in northern Tibet, western China: constraints on the exhumation of the central Qiangtang metamorphic belt. Lithos 121, 167–175.
Zhao, G.C., Wang, Y.J., Huang, B.C., Dong, Y.P., Li, S.Z., Zhang, G., Yu, S., 2018. Geological reconstructions of the East Asian blocks: from the breakup of Rodinia to the assembly of Pangea. Earth Sci. Rev. 186, 262–286.
Zhao, P.L., Chu, X., Williams-Jones, A.E., Mao, J.W., Yuan, S.D., 2022. The role of phyllosilicate partial melting in segregating tungsten and tin deposits in W-Sn metallogenic provinces. Geology 50, 121–125.
Zhu, J.-J., Hu, R.-Z., Bi, X.-W., Zhong, H., Chen, H., 2011. Zircon U–Pb ages, Hf–O isotopes and whole-rock Sr–Nd–Pb isotopic geochemistry of granitoids in the Jinshajiang suture zone, SW China: constraints on petrogenesis and tectonic evolution of the Paleo-Tethys Ocean. Lithos 126, 248–264.
Zhu, D.-C., Zhao, Z.-D., Niu, Y., Dilek, Y., Hou, Z.-Q., Mo, X.-X., 2013. The origin and pre-Cenozoic evolution of the Tibetan Plateau. Gondwana Res. 23, 1429–1454.
Zhu, J.-J., Richards, J.P., Rees, C., Creaser, R., DuFrane, S.A., Locock, A., Petrus, J.A., Lang, J., 2018. Elevated magmatic sulfur and chlorine contents in ore-forming magmas at the Red Chris Porphyry Cu-Au Deposit, Northern British Columbia, Canada. Econ. Geol. 113, 1047–1075.
Zi, J.-W., Cawood, P.A., Fan, W.-M., Tohver, E., Wang, Y.-J., McCuaig, T.C., 2012a. Generation of Early Indosinian enriched mantle-derived granitoid pluton in the Sanjiang Orogen (SW China) in response to closure of the Paleo-Tethys. Lithos 140–141, 166–182.
Zi, J.W., Cawood, P.A., Fan, W.M., Wang, Y.J., Tohver, E., 2012b. Contrasting rift and subduction-related plagiogranites in the Jinshajiang ophiolitic mélange, Southwest China, and implications for the Paleo-Tethys. Tectonics 31, TC2012. https://doi.org/10.1029/2011TC002937.
Zou, X.Y., Qin, K.Z., Han, X.L., Li, G.M., Evans, N.J., Li, Z.Z., Yang, W., 2019. Insight into zircon REE oxy-barometers: a lattice strain model perspective. Earth Planet. Sci. Lett. 506, 87–96.